Zhang, L., Werner, M. J., & Goda, K. (2018). Spatiotemporal Seismic Hazard and Risk Assessment of Aftershocks of M 9 Megathrust Earthquakes. *Bulletin of the Seismological Society of America*, *108*(6), 3313-3335. https://doi.org/10.1785/0120180126

Spatiotemporal Seismic Hazard and Risk Assessment of Aftershocks of M9 Mega-Thrust Earthquakes

Lizhong Zhang[1], Maximilian J. Werner[2], and Katsuichiro Goda[1]

[1]Department of Civil Engineering, University of Bristol, Queen's Building, Bristol BS8 1TR, United Kingdom

[2]School of Earth Sciences and Cabot Institute, University of Bristol, Wills Memorial Building Queens Road, Bristol BS8 1RJ, United Kingdom

Corresponding Author: Lizhong Zhang

Corresponding Author E-mail: lz0560@bristol.ac.uk

Abstract

Current national seismic hazard models neglect time-dependent hazard due to triggered earthquakes, although these can certainly generate damaging ground motions. To understand the relative importance of aftershock hazard and risk in the context of a mega-thrust subduction-zone earthquake, we develop a new simulation framework for spatiotemporal seismic hazard and risk assessment of a mega-thrust earthquake and its aftershocks along the plate boundary and in the onshore continental crust. Tohoku region in the northeast Japan is considered as an example to show how the new simulation framework can be implemented to assess the spatiotemporal hazard and risk of aftershocks triggered by a **M**9 Tohoku-like earthquake. We generate quasi-3D synthetic aftershock catalogs using the Epidemic Type Aftershock Sequences (ETAS) model, modified to characterize aftershocks of large and anisotropic finite mainshock sources. By including the mainshock source model in the new simulation framework, the uncertainty of generating synthetic aftershock catalog is small in comparison with the observation. Therefore, should the mainshock source model is available right after the mainshock, the new simulation framework can be used for the quasi-real time hazard and risk assessments of aftershocks in different regions. For Tohoku region, we assess the relative importance of subduction-zone versus onshore-crustal aftershocks. The results show that the subduction-zone aftershocks tend to dominate hazard with peak ground velocity (PGV) < 60 cm/s (the boundary between VIII (severe) and IX (violent) of Modified Mercalli Intensity). On the other hand, onshore-crustal aftershocks control extreme hazards exceeding PGV of 60 cm/s. Moreover, on the day of the mainshock, aftershocks contribute about 23% of the onshore hazard with PGV > 60 cm/s, and the aftershock hazards remain relatively high for 4-5 days depending on different sites. From a seismic risk viewpoint, the subduction-zone and onshore-crustal aftershocks in the mega-thrust sequence affect buildings differently; both have similar potential to cause minor damage, whilst the latter tend to cause more severe damage.

Introduction

Recent great earthquakes along subduction zones have triggered numerous aftershocks over many years and regions of hundreds of kilometers. Seismicity rates are increased by orders of magnitude not just along the ruptured plate interface, but also at population centers in the overriding continental crust. Despite the obvious seismic hazard and risk to people and infrastructure, current seismic hazard models largely neglect the influence of time-dependent aftershock triggering and secondary earthquake clustering. This influence is important, however, for decision-making in post-earthquake risk management, including humanitarian relief, building tagging, inspection prioritization, retrofitting, and informing the population of residual risks (e.g., Jordan and Jones, 2010; Jordan *et al.*, 2011).

The 2011 Tohoku earthquake sequence exemplifies this secondary hazard and risk in the onshore crust. The sequence started on March 9, 2011, with the **M**7.3 foreshock, followed on March 11 by the **M**9 mainshock, which ruptured a 530 km × 200 km fault plane (Yagi and Fukahata, 2011) between the Pacific and North American Plates in the northeast offshore region of Japan. In total, more than 200 aftershocks with depths less than 100 km and Japan Meteorological Agency (JMA) magnitude $\mathbf{M}_j$ greater than 5.5 occurred within 100 days of the mainshock. Amongst the five $\mathbf{M}_j \geq 7$ aftershocks, three occurred along the plate interface, one in the subducting slab, and one in the shallow continental crust on April 11. The latter ruptured the Yunodake and Itozawa faults in Fukushima Prefecture at a distance of 300 km from the epicenter of the mainshock (Fukushima *et al.*, 2013; Toda and Tsutsumi, 2013), and the aftershock triggered its own cascade of secondary aftershocks.

While stochastic models of seismicity cascades certainly exist, their current formulations are not well suited to accurately assess the seismic hazard and risk of quakes triggered by a great mega-thrust earthquake in a subduction zone setting. First, most models of clustered seismicity are two-dimensional, which is problematic for accurate hazard calculations

for subduction zones having complex 3D geometry. Second, many models employ spatial distributions of aftershocks that are isotropic around the mainshock epicenter, constituting a poor representation of the aftershock zones of great subduction earthquakes. Third, models typically neglect available scaling laws of the rupture areas of great earthquakes, even though they constrain the aftershock zone strongly. For instance, the Epidemic Type Aftershock Sequences (ETAS) model is widely used to forecast the spatiotemporal seismicity rate for crustal seismicity (Kagan and Knopoff, 1987; Ogata, 1988, 1998; Lombardi and Marzocchi, 2010; Werner *et al.*, 2011; Zhuang, 2011; Gerstenberger *et al.*, 2014; Marzocchi *et al.*, 2014; Field *et al.*, 2017a). Conventionally, an isotropic power law is used in the ETAS model. Ogata (1998) and Zhuang *et al.* (2004) used a 2D Gaussian distribution to model the anisotropy of the aftershocks. However, the spatial distribution of aftershocks may be better represented by a power law, which decays more gradually than the Gaussian distribution in the far field (Felzer and Brodsky, 2006). This is related to the agreement of the static stress triggering and spatial aftershock with power-law decay (Toda et al., 2011; Hainzl et al., 2014). In this study, we develop a new spatially anisotropic aftershock kernel that combines a simulated 2D mainshock rupture area (from scaling laws) with a power-law beyond the rupture. This new formulation is important because seismic hazard and risk due to triggered crustal events are sensitive to the spatial distribution of aftershocks near the rupture boundary in the continental crust, where buildings and other infrastructure are nearby.

The importance of aftershocks in seismic hazard has been highlighted previously. For instance, Marzocchi and Taroni (2014) concluded that aftershocks should be included in probabilistic seismic hazard analysis (PSHA), because only using the PSHA result from the declustered catalog underestimated hazard rates. Approaches for including aftershocks can be distinguished by the treatment of mainshocks: (1) long-term (years to centuries), time-independent approaches that integrate aftershock hazard on unconditional mainshock

98 occurrence; (2) short-term (days to years) approaches that estimate aftershock hazard
99 conditional on a specified mainshock source.

100 Several studies have implemented the former approach. For example, Toro and Silva
101 (2001) first incorporated earthquake clustering into PSHA. They assumed an earthquake
102 sequence could be modelled by the probabilities of unions of events exceeding a specific
103 ground motion level and each event was assumed to be independent in time for the New Madrid
104 Seismic Zone (NMSZ). This approach was further applied by Boyd (2012) to gridded hazard
105 curves in San Jose, California. Boyd (2012) showed the hazard curves (PGA and Spectral
106 Acceleration (frequency=1 Hz)) from the U.S. 2008 National Seismic Hazard Maps were
107 increased by 10%-20% when aftershocks were included.

108 The latter approach requires detailed mainshock source models but would be effective
109 for the short-term decision-makings and has been applied globally for the crustal seismicity.
110 Yeo and Cornell (2009) developed a time-dependent aftershock probabilistic seismic hazard
111 analysis using the modified Omori law combined with an empirical scaling relationship for
112 rupture area (e.g., Wells and Coppersmith, 1994). Their seismicity source model did not
113 account for secondary aftershock occurrences, thus underestimating locally concentrated
114 seismicity and its hazard in the far field. Yaghmaei-Sabegh *et al.* (2017) conducted cluster-
115 based PSHA using a temporal ETAS model. The uniform aftershock spatial distribution was
116 considered given linear faults of M7-level earthquakes for NMSZ. The temporal ETAS model
117 from Yaghmaei-Sabegh *et al.* (2017) considered multiple generations of aftershocks rather than
118 the Modified Omori law. Iervolino *et al.* (2015) and Field *et al.* (2017b) developed operational
119 earthquake loss forecasting in Italy and California, respectively, based on spatiotemporal ETAS
120 earthquake clustering models of (shallow) clustered seismicity (Marzocchi *et al.*, 2014; Field
121 *et al.*, 2017a). None of these studies, however, assessed the seismic effects of great mega-thrust
122 earthquakes. It should be noted that the latter approach is useful for aftershock scenarios of

megathrust events for different regions. The source modeling is general, because it's only constrained by empirical scaling laws and reasonable subduction zone geometric constraints.

This study develops a new framework to conduct spatiotemporal seismic hazard and risk assessments focusing on a **M**9 mega-thrust event triggering moderate-to-large aftershocks (**M** ≥ 5.5) along the plate interface and in the continental crust. We investigate the importance of the aftershock sequence in terms of ground motion intensity and seismic fragility. Our target region is northeast Japan to demonstrate how the new framework can be applied in a subduction zone. The novelties of this study are twofold. First, we employ the ETAS model (Ogata and Zhuang, 2006; Zhuang, 2011; Seif *et al.*, 2017) to model aftershock cascades of a **M**9 mega-thrust earthquake. Second, we model the spatial distribution of major aftershocks with an appropriate anisotropic power-law kernel, a mainshock rupture zone constrained by empirical length-width scaling laws, and the empirical depth profile. The limitation of the new simulation framework is that to reduce the uncertainty of the synthetic aftershock catalog, the mainshock source parameters are necessary. Therefore, the new simulation framework is applicable for quasi-real time hazard assessment immediately after the mainshock source model is available. Otherwise, different mainshock rupture scenarios should be considered for the region without observation. The objectives of this paper are: 1) to develop a tool by convolving the ETAS model, ground motion prediction equation (GMPE), and seismic fragility model to enable more risk-informed decision-making in post-earthquake situations of mega-thrust events, 2) to show the new framework could capture the M9 observed megathrust earthquake sequence in Japan, and 3) to conduct seismic hazard and risk analyses at different onshore sites for Japan using the new simulation framework.

Data

Since northeast Japan is the target region, specific catalogs are selected for different purposes. (1) To estimate parameters of the ETAS model, we use the JMA catalog (see the Data and Resources section). (2) To consider the uncertainty of the source parameters of the 2011 Tohoku mainshock, we use the locations from the ANSS (Advanced National Seismic System), global Centroid Moment Tensor (gCMT), International Seismological Center (ISC), and JMA (see the Data and Resources section). (3) To model the 3D rupture areas of the large aftershocks, we use depths of past events from the JMA catalog, the slab model of the Japan Trench from Hayes *et al.* (2012), and focal mechanisms from the gCMT catalog. (4) To show the comparison between simulated peak ground velocity (PGV) and observed PGV, the ground motion data are taken from Goda *et al.* (2015). The ground motion records in this study are from the K-NET, KiK-net (National research Institute for Earth science and Disaster resilience), and SK-net (Earthquake Research Institute) (see the Data and Resources section). The selected strong motion stations with near-surface ground information, the distances to the target sites, and the available number of records are summarized in **Table 1**.

Overview of Framework

The framework for spatiotemporal seismic hazard and risk assessment due to a mega-thrust subduction earthquake sequence consists of a seismicity model, seismic hazard analysis, and seismic risk analysis, and is illustrated in **Figure 1**. Although the target region is northeast Japan in this study, the framework is applicable to other subduction zones (e.g., Indonesia and Chile). We adopt the spatiotemporal ETAS model as the seismicity source model; this constitutes the key technical element in the framework. The parameters of the ETAS model are estimated from earthquake catalogs. The calibrated ETAS model generates realistic synthetic mainshock-aftershock sequences that capture observed aftershock rates in space and time.

171 Additional features including rupture dimensions, depths, earthquake types, and focal
172 mechanisms are assigned in the synthetic catalogs.

173 In addition, earthquakes with the same magnitude can have different ground motion
174 characteristics in terms of duration and frequency content. Building damage assessments are
175 sensitive to these characteristics. For this reason, we use a GMPE developed for subduction
176 earthquakes and crustal earthquakes to calculate their specific ranges of seismic intensities. In
177 our study, 'crustal earthquakes' refer to the onshore-crustal events with depths less than 30 km
178 in the continental crust, and 'subduction earthquakes' refer to the subduction-zone events that
179 take place on (near) the subduction plate interface. Next, we integrate the space-time aftershock
180 rate of the ETAS model with the GMPE to assess the time-dependent seismic hazard at multiple
181 sites in terms of daily rates of seismic intensity exceeding a certain threshold.

182 Different comparisons of the observed and synthetic catalogs can be carried out. For
183 example, we compare the daily exceedance rates of observed and simulated ground motions,
184 and we assess the relative importance of crustal and subduction earthquakes in terms of ground
185 motions. In addition, we compare the time-dependent hazard rates with the long-term hazard
186 rates in the target region to assess the importance of the triggered aftershocks.

187 Seismic risk analysis evaluates the probabilities of occurrence of consequences in
188 building damage and loss given a major event or sequence (McGuire, 2004). Seismic risk
189 analysis is useful for decision-making in the short- and long-term. A viable approach to
190 assessing seismic risk from seismic hazard is using fragility curves, which we employ here to
191 show how the spatiotemporal hazard can be accommodated in the seismic risk analysis.

192 In the following, we first describe the new generic framework including parameter
193 estimation and catalog simulations of the ETAS model in the Spatiotemporal ETAS Model
194 section. Then we consider northeast Japan as the target region and present the procedures and

results of the seismicity model, hazard analysis, and risk analysis for **M**9 earthquake sequences offshore Japan.

Spatiotemporal ETAS Model

ETAS model

The total seismic rate $\lambda(t,x,y|H_t)$ of the spatiotemporal ETAS model consists of a background rate $\mu(x,y)$ and a triggering rate $g(t-t_j, x-x_j, y-y_j; M_j)$ at time t and location (x,y) (Zhuang, 2011; Seif *et al.*, 2017), and can be expressed as follows:

$$\lambda(t,x,y|H_t) = \mu(x,y) + \sum_{j:t_j<t} g(t-t_j, x-x_j, y-y_j; M_j) \quad (1)$$

where H_t represents the historical seismicity up to time t ($H_t = \{x_j, y_j, t_j, M_j\}; t_j<t$). The triggering function $g(t,x,y;M)$ includes the productivity ($K_0\, e^{\alpha(M-M_{cut})}$), the normalized modified Omori law $v(t)$, and a spatial distribution $f(x,y|M)$ of seismic events:

$$g(t,x,y;M) = K_0\, e^{\alpha(M-M_{cut})} \cdot v(t) \cdot f(x,y|M) \quad (2)$$

where M_{cut} is the cut-off magnitude to select earthquakes larger than M_{cut}. K_0 (event/day) and α (magnitude^{-1}) are the productivity parameters. α determines how the triggering productivity of an earthquake increases with magnitude, whereas K_0 measures the intensity of aftershock generation, defining the number of triggered events above M_{cut}.

The temporal distribution is the normalized modified Omori law:

$$v(t) = c^{p-1}(t+c)^{-p}(p-1) \quad (3)$$

where c (day) and p are parameters. c is applied to eliminate a singularity at $t = 0$ and affected by the number of events in the catalog during the early phase of the aftershock process (Seif *et al.*, 2017). The p-value is associated with the decay rate of aftershocks in time; the decay rate increases with the p-value.

The spatial distribution of triggered events is defined by:

$$f(x,y|M) = \frac{(q-1)}{\pi\left(x^2+y^2+d\ e^{\gamma(M-M_{cut})}\right)}\left(1+\frac{x^2+y^2}{d\ e^{\gamma(M-M_{cut})}}\right)^{-q} \quad (4)$$

where d (km^2), q, and γ (magnitude^{-1}) are parameters. $d\ e^{\gamma(M-M_{cut})}$ is a measure of the source dimension and scales the spatial aftershock footprint, whereas q describes the spatial decay of aftershocks.

ETAS parameter estimation

The ETAS parameters are estimated by using the maximum likelihood estimation (MLE) method (Zhuang, 2011; Seif *et al.*, 2017). To estimate the parameters of the ETAS model reliably, the input earthquake catalog needs to be complete and homogeneous over an appropriate target window. The target window is a specific range of space, time, and magnitude to filter seismic events. However, some events outside the target window may trigger seismic events in the target window. Therefore, an auxiliary window is often introduced to reduce the bias, which is larger than the target window, and the combination of the auxiliary and target windows is referred to as data window (Wang *et al.*, 2010).

The log-likelihood function can be expressed as:

$$logL = \sum_{i=1}^{n} \log\left(\lambda\left(t_i, x_i, y_i \middle| H_{t_i}\right)\right) - \int_s \int_0^T \lambda(t,x,y)dt\ dx\ dy \quad (5)$$

where n is the number of events in the target window, and S and T are the spatial and temporal ranges of the target window.

ETAS simulation

The conventional ETAS model distributes aftershocks isotropically around a mainshock epicenter, which is more applicable to **M**7-class earthquake sequences, and less to **M**8-9 mega-thrust subduction events. For example, according to Ogata and Zhuang (2006), the performances of the isotropic and anisotropic spatial distributions are similar for the offshore Tohoku region from 1926 to 1995 with a maximum $\mathbf{M}_j$ = 7.9 in the historical catalog. In addition, recent empirical scaling laws by Thingbaijam *et al.* (2017) indicate that differences

between fault width and fault length of subduction-interface events are indistinguishable when **M** < 7.5. When the magnitude exceeds **M**8, however, the fault length is generally greater than the fault width.

We modify the ETAS simulation approach of Seif *et al.* (2017) to capture the spatial distribution of aftershocks of a **M**9 Tohoku-like subduction-zone earthquake. We divide the first generation of aftershocks into two groups: the first group occurs in the mainshock rupture area, while the second group obeys a power-law decay with distance beyond the rupture area. Subsequent generations of triggered events follow the isotropic power law in Equation (4) to mimic isotropic secondary clustering. The proportions of the aftershocks inside and outside of the rupture area are determined based on the observed spatial distribution of aftershocks (e.g., the 2010 Maule earthquake sequence and the 2011 Tohoku earthquake sequence). We simulate variations in the mainshock rupture area and geometry to account for their uncertainty in future mega-thrust earthquakes. The 2D mainshock rupture area is obtained from sampled rupture lengths and widths constrained by empirical relationships. Strike and dip angles are based on different focal mechanism solutions (e.g., from gCMT and the U.S Geological Survey) of the same historical **M**9 event in the target region.

The first-generation aftershocks inside and outside the rupture area are distributed using a 2D uniform distribution and power law kernels (Vere-Jones, 1992; Woo, 1996), respectively. The 2D uniform distribution implies that any location inside the rupture area is equally ready for an aftershock. After several attempts of approximating Tohoku's anisotropic spatial distribution with a single kernel (e.g. anisotropic Gaussians with various variance scaling functions), we found that this combination can capture the observed characteristics much better. Other attempts, i.e. the 2D Gaussian and anisotropic kernel distributions, are provided in Appendix 1. Several authors (Das and Henry, 2003; Asano *et al.*, 2011; Rietbrock *et al.*, 2012) inferred relations between slip and aftershocks, but they are not yet ready for

implementation because (i) a slip model forecast is required, (ii) the relations are currently qualitative and occasionally debatable, and (iii) the relations do not usually apply to off-fault aftershocks. Although aftershocks within the rupture area of mega-thrust earthquakes are not usually distributed uniformly, the observed clustering appears well approximated by secondary aftershocks that cluster around the first generation of uniformly distributed aftershocks.

To be consistent with the empirically-supported power-law decay in the far field (Felzer and Brodsky, 2006; Toda *et al.*, 2011; Hainzl *et al.*, 2014), we developed a power-law component with distance from the rupture area. To this end, we modeled seismicity decay perpendicularly to the four edges of the rectangle using the 1D power law, and seismicity decay in the four corners of the rectangle as quarter circles of a 2D power law. The 1D power law is given by:

$$k_{1d}(x_{1d}, y_{1d}) = Beta(q - 0.5, 0.5)^{-1} h^{-1} (1 + \frac{x_{1d}^2 + y_{1d}^2}{h^2})^{-q} \quad (6)$$

while the 2D power law is described by:

$$k_{2d}(x_{2d}, y_{2d}) = \frac{q-1}{\pi h^{-2}} (1 + \frac{x_{2d}^2 + y_{2d}^2}{h^2})^{-q} \quad (7)$$

where q is the power-law exponent, h (km) is the kernel bandwidth, and *Beta*(•) is the beta function. An example of the resulting spatial probability density function (PDF) of (first-generation) aftershocks of a mainshock rupture with 500 km length and 300 km width is displayed in **Figure 2**. x_{1d}, y_{1d}, x_{2d}, and y_{2d} are the locations of aftershocks outside the rupture area with $\pm\frac{500km}{2}$ in x (rupture length) and $\pm\frac{300km}{2}$ in y (rupture width). We assign the exponent q of the power laws the same value as the exponent of the isotropic decay in Equation (4). Therefore, the decay rates of the anisotropic and isotropic spatial aftershock distributions are identical in the far field.

290 *Earthquake rupture model*

291 The outputs of the ETAS simulations are the synthetic catalogs including occurred times,
292 locations of epicenters, and magnitudes of the events. As indicated in the Overview of section,
293 we assign additional features including the depth, earthquake type, and focal mechanism to
294 each simulated earthquake. This is described in detail next.

295 Depths for earthquakes with **M**<8 are sampled from empirical cumulative distribution
296 functions (ECDFs) of depth that are obtained based on an instrumental catalog. We divide the
297 target window into sub-regions with 10 km width from the trench line to the continental crust
298 to estimate the ECDFs of depth in each sub-region. Past earthquakes **M**≥5 are used. The events
299 with depths less than 5km are eliminated because the majority of these events are remote events
300 and poorly estimated with depths 0km. It should be noted that the 0km depth shows the depth
301 of earthquake is not constrained by the JMA monitoring system, so using 0km depth could
302 potentially overestimate the hazard results. Bins with a small number of events (< 20) are
303 combined with the closest bin to avoid insufficient events for defining the ECDFs of depth. In
304 addition, all simulated earthquakes with **M**≥8 are treated as subduction-interface earthquakes
305 and the depths are assigned directly from a slab model. This is because the largest historical
306 crustal earthquake in Japan is less than **M**8. Kanaori *et al.* (1991) listed the destructive
307 earthquakes from 715 to 1984 with **M**≥6.4 for Japan. The largest magnitude for inland Japan
308 is the **M**8.0 Nobi earthquake. In addition, the historical large crustal earthquakes in other
309 regions (e.g., Mexico) could be 7.5≤**M**≤7.8 (Suárez *et al.*, 1994). For the crustal seismicity in
310 California, Field *et al.* (2017) also consider the maximum magnitude of magnitude frequency
311 distribution with 8.

312 Earthquake types (continental-crust, subduction plate-boundary, or subduction intra-
313 plate) are defined by the sampled depths and the slab model: earthquakes more than 20 km
314 above the plate interface are defined as crustal earthquakes, the layer within ±20km of the plate

315 interface is assumed to contain subduction-interface earthquakes (allowing for depth
316 uncertainty), and remaining earthquakes are treated as intra-slab earthquakes.

317 To obtain the range of strike and dip angles for crustal and subduction earthquakes, we
318 use **M**5.5+ earthquakes in the gCMT catalog in the target window. We assume the strike and
319 dip angles of the subduction aftershock are similar to the strike and dip angles of the subduction
320 plane in Eastern Japan. Therefore, the strike and dip angles of nodal planes 1 and 2 that are
321 close to the strike and dip angles of subduction plane are selected. For crustal aftershocks, the
322 strike angle of historical shallow crustal earthquakes and active faults with depths less than
323 15km has a good agreement with the strike angle of the subduction plane. For example, the
324 1998 **M**6.3 Iwate earthquake (strike angle=216º), the 2003 **M**6.1 northern Miyagi earthquake
325 (strike angle=203º), and the 2008 **M**6.9 Iwate-Miyagi Nairiku earthquake (strike angle=209º)
326 (Nakahara *et al.*, 2002; Miura *et al.*, 2004; Asano and Iwata, 2011). In addition, according to
327 Japan Seismic Hazard Information Station (JSHIS) (http://www.j-shis.bosai.go.jp/en/), the
328 strike angles of the Nagamachi-Rifu-sen fault, the Fukushima-bonchi-seien fault, and the
329 Nagai-bonchi-seien fault are 231.9º, 212.6º, and 186.7º, respectively. Therefore, we select the
330 strike angle which is close to the strike angle of subduction plane from two node planes of the
331 crustal event. The ECDFs of strike and dip angles for crustal and subduction earthquakes are
332 evaluated, and the simulated angles are assigned to the large aftershocks with **M**≥6.5.

333 To simulate ground motions, we require the shortest distance between a source and a
334 site. The source models depend on magnitude and location. We do not simulate the finite
335 rupture planes of **M**<6.5 earthquakes, and so calculate the distance to the hypocenter.
336 Simulated **M**≥8 earthquakes are constrained to the plate interface, and we calculate distances
337 to the nearest point on the simulated (finite) rupture plane. Source models for **M**≥6.5 crustal
338 and subduction-interface aftershocks are generated from empirical scaling laws and the
339 empirical distributions of strike and dip angles. The slab model provides the boundary of the

projected 2D rupture area of interface earthquakes, while the finite rupture planes of crustal aftershocks are simulated based on the source model.

In the next two sections, we show the specific results associated with the target region of Tohoku, Japan from seismicity analysis to hazard and risk analysis.

Seismicity Analysis of M9-triggered Aftershock Sequences in Tohoku

ETAS parameter estimation in Tohoku

The ETAS parameter estimation requires a homogeneous catalog, therefore the JMA catalog is used as it has a unified magnitude scale $\mathbf{M}_j$ and a low magnitude of completeness in Japan. The spatial target and data windows of the ETAS parameter estimation are shown in **Figure 3**a. The target window encompasses the rupture area of the 2011 Tohoku mainshock, its aftershock field, and onshore regions to include events in the continental crust. The data window is larger than the target window by a 2º extension along all sides of the target window. Because we focus on future mega-thrust subduction events triggering subduction aftershocks and crustal aftershocks in the subducting plate and overriding crust, respectively, the selected historical events in the target window include not only the 2011 Tohoku sequences but also other large subduction and crustal earthquakes before 2011. More specifically, we select events between January 1, 1970, and December 31, 2015 and with depths less than 100 km without setting a magnitude threshold which leads to 83000+ events in total.

The temporal completeness M_c is estimated in a sliding time window of 200 events using the method suggested by Amorèse (2007) and Seif *et al.* (2017) from 1970 to 2015 (**Figure 3**b). Due to missing aftershocks immediately after the Tohoku mainshock, M_c briefly increases to $\mathbf{M}_j$ 5.3. In this study, M_{cut} is set to 4.7 for seismic hazard analysis, because a large offshore region is selected in the target and data windows which leads to a high magnitude of completeness during the 2011 Tohoku sequence. In addition, M_{cut} is kept constant to reduce

365 the bias in the ETAS simulation (Harte, 2015). This also allows the direct application of the
366 GMPE by Morikawa and Fujiwara (2013) in subsequent seismic hazard analyses, which is
367 applicable to events with **M**≥5.5 in Japan. Selecting a lower magnitude cut-off with 4.7 rather
368 than the GMPE threshold of 5.5 in the ETAS simulation is beneficial to assess the potential of
369 **M**4.7 earthquakes for triggering **M**≥5.5 aftershocks. The *b*-value estimation with 5%-95%
370 percentiles (Aki, 1965; Shi and Bolt, 1982) of the selected events from 1970 to 2015 with
371 M_{cut}=4.7 is displayed in **Figure 3**c. The 2D histogram of observed events in the 100 days after
372 the 2011 Tohoku mainshock with **M**≥5.5 is shown in **Figure 3**d.
373 Because the empirical laws of triggered seismicity are thought to be reliable (e.g., the
374 Gutenberg-Richter law and the modified Omori law), ETAS parameters are expected to be
375 robust given a complete and sufficiently large catalog. We investigate the sensitivity of the
376 ETAS parameters by considering two time periods: Case 1 covers 1970-2015 (3568 events),
377 while Case 2 (1725 events) comprises the 2011 Tohoku sequence only (see **Table 2**).
378 The mean estimates of the parameters together with their standard errors for Cases 1
379 and 2 are shown in **Table 3**. The productivity parameters α and K_0 change slightly between
380 Cases 1 and 2. When data that exhibit an anisotropic aftershock distribution after a large
381 mainshock are fitted with the isotropic distribution of the ETAS model, K_0 and α tend to be
382 overestimated and underestimated, respectively, as in Cases 1 and 2 (Hainzl *et al.*, 2013).
383 Due to the bias in the productivity parameters, we conduct the third parameter
384 estimation (Case 3). The same earthquake catalog as Case 1 is used, and the temporal and
385 auxiliary windows of Case 3 are summarized in **Table 2**. As suggested by Helmstetter *et al.*
386 (2005), Hainzl *et al.* (2013), and Seif *et al.* (2017), K_0 is estimated with fixed $\alpha = 2.3$ to ensure
387 the productivity of the simulated catalogs is similar to that of the catalog.
388 The temporal parameters *c* and *p* differ significantly between Cases 1 and 2. It seems
389 likely that the short window of Case 2 and missing early aftershocks lead to biased *c* and *p*-

values. We also compare the values with those estimated by Ogata and Zhuang (2006). Ogata and Zhuang (2006) obtained *c* and *p*-values of 0.0243 and 1.050, respectively, with $M_c = 4.5$ for the offshore Tohoku region (see Table 2 in Ogata and Zhuang (2006)). Their *c* value is essentially identical to ours, but their *p*-value is much smaller. We presume that their temporal window extends too far back to be complete offshore (Nanjo *et al.*, 2010), and thus the aftershock decay may be less well captured.

The final parameter set that is used to simulate catalogs is summarized as Case 4 in **Table 3**. The ETAS parameters in Case 4 are chosen from Cases 1 and 3. The parameters that are relatively independent of magnitude in space and time (i.e. *c*, *p*, *d*, and *q*) are taken from Case 1. The spatial parameter γ is also from Case 1, as the spatial distribution of aftershocks triggered by the mainshock is used to simulate the subsequent generation of aftershocks. The value of K_0 is selected from Case 3 estimated with a fixed $\alpha = 2.3$ since α is underestimated in the parameter estimation of Cases 1 and 2.

ETAS simulation in the Tohoku region

We generate synthetic catalogs as described in the Spatiotemporal ETAS Model section and validate the simulations by comparing daily average numbers of simulated events with the actual 2011 Tohoku sequence. We constrain the simulations to mimic the Tohoku sequence as follows. First, a **M**9 earthquake initiates the aftershock sequences. We account for the uncertainty of the mainshock source in terms of magnitude, epicenter, strike, and dip. (1) The magnitude of the mainshock is sampled from a uniform distribution between **M**8.95 and **M**9.05. (2) The epicenter is simulated randomly from a 2D Gaussian distribution that is fit to the four location estimates of the 2011 Tohoku mainshock by the ANSS (38.2970°N,142.3730°E), gCMT (38.3200°N,142.3700°E), ISC (38.2963°N,142.4980°E), and JMA (38.1035°N,142.8610°E) catalogs. To ensure that the rupture area of the mainshock is on the subduction interface and does not extend beyond the trench, the simulated epicenter of the

mainshock is constrained to lie farther than 150 km from the trench. The threshold distance of 150 km corresponds to a half of the maximum rupture width of 300 km of a bilateral rupture. (3) The dip and strike angles are sampled from uniform distributions between 10º-13º and 195º-203º, respectively, selected from available rupture models of the Tohoku earthquake (Koketsu *et al.*, 2011; Shao *et al.*, 2011; Suzuki *et al.*, 2011; Yagi and Fukahata, 2011). (4) The rupture lengths and widths are sampled from the empirical scaling laws of Thingbaijam *et al.* (2017) with a covariance between rupture length and width from Goda *et al.* (2016). By having the sampled epicenter, and strike and slip angles, the location of the rupture area is calculated assuming a bilateral rupture. We divide the first-generation aftershocks into those triggered within the (2D) rupture plane and those triggered outside the rupture plane according to the observed partitioning during the Tohoku sequence: about 90% of aftershocks are projected onto the rupture area, while 10% occur outside. Finally, we capture the uncertainty of the ETAS parameters by sampling parameters from normal distributions with means and standard errors from Case 4 in **Table 3**. Following the simulation procedures that are described above, 100,000 synthetic **M**4.7+ catalogs are simulated over a one-year period in this study.

To illustrate the ETAS model's ability to mimic the 2011 Tohoku sequence, we compare simulations with observations. First, we compare observed and simulated magnitude-frequency distributions (MFD) above **M**5.5 in the first 100 days in **Figure 4**a. The observed MFD falls into the range of simulated MFDs. Second, we compare the daily numbers of observed and simulated events over 30 days in **Figure 4**b, again finding good agreement between the observations and the range of simulations. Third, to inspect spatial agreement, we show two examples of simulations with mainshock rupture areas similar to the 2011 Tohoku earthquake. In **Figure 5**a and c, we show the spatial aftershock rates of two single simulations over 100 days with **M**≥5.5 (to be compared with **Figure 3**d); the spatial distributions show qualitative agreement. In **Figure 5**b and d, the daily number of events of the two simulations

440 is compared with the observed daily number of events, exhibiting good agreement. In the figure
441 panels, the sampled mainshock epicenter, strike and slip angles, and rupture area for each
442 simulation are also included.
443

444 ## Seismic Hazard Analysis of M9-triggered Aftershock Sequences in Tohoku

445 We select a GMPE and seismic fragility model appropriate for Japan. We use a GMPE
446 developed by Morikawa and Fujiwara (2013). Compared with other GMPEs (Zhao *et al.*, 2006;
447 Abrahamson *et al.*, 2014, 2016) that calibrate parameters from global ground motion records,
448 the GMPE from Morikawa and Fujiwara (2013) is only calibrated on Japanese ground motion
449 records, including the 2011 Tohoku sequence. In addition, the latest GMPE for subduction
450 earthquakes (Abrahamson *et al.*, 2016) does not provide PGV, which is the potential required
451 input for Japanese fragility curves. The general required input for Japanese fragility curves is
452 JMA intensity (I_{JMA}), peak ground acceleration (PGA), or peak ground velocity (PGV)
453 (Yamaguchi and Yamazaki, 2001; Midorikawa *et al.*, 2011). However, the standard deviation
454 of PGA is higher than I_{JMA} and PGV (Yamaguchi and Yamazaki, 2001; Wu *et al.*, 2016), and
455 I_{JMA} as an intensity measure is only widely used in Japan. Therefore, we use PGV in this study.
456 The median values of PGV for subduction and crustal earthquakes from Morikawa and
457 Fujiwara (2013) with V_{s30} = 300 m/s are shown in **Figure 6**(a) and (b), respectively. An existing
458 seismic fragility model of wood-frame houses for Japan by Yamaguchi and Yamazaki (2001)
459 is used to evaluate the probabilities of reaching different damage states. The slight, moderate,
460 and heavy damage are referred to as damage state 1 (DS1), damage state 2 (DS2), and damage
461 state 3 (DS3), respectively. The fragility curves in terms of PGV are shown in **Figure 6**(c).
462 This study does not estimate the cumulative damage due to triggered aftershocks, because the
463 fragility curve of aftershocks is not available in Japan.

The required inputs for the GMPE from Morikawa and Fujiwara (2013) are magnitude, source distance, type of event, and time-averaged shear-wave velocity in the uppermost 30 m (V_{s30}) of the site. The magnitude is from the synthetic catalogs, and the earthquake type and the source distance are estimated using available local catalogs (see the Earthquake rupture model section). $\mathbf{M}_j$ is converted to **M** using empirical equations by Scordilis (2005) because the magnitude type input to the GMPE is moment magnitude. V_{s30} = 200 m/s, 300 m/s, and 400 m/s are used to investigate the effects of different soil conditions. To consider the uncertainty of the GMPE, the PGV is sampled given the inter-event sigma and intra-event sigma from the lognormal distribution (Morikawa and Fujiwara, 2013). The ratio of inter-event sigma and intra-event sigma is taken from Zhao *et al.* (2006). Inter-event sigma is the variability for different events, and intra-event sigma is the variability for different record stations of the same event (Youngs *et al.*, 1995). Therefore, in the simulation the same inter-event variability is used for the same event at different sites.

In this study, three sites are considered for seismic hazard and risk calculations, due to the potential high seismic risk, and the subsequent social and economic impact in the region: Sendai City (141.0286ºE, 38.3072ºN) in Miyagi Prefecture, Fukushima Daini Nuclear Power Plant (Fukushima II NPP) site (141.0132ºE, 37.3236ºN) in Fukushima Prefecture, and Tokyo (139.7679ºE, 35.7235ºN) in Tokyo Metropolis (see **Figure 3**a). Sendai is the capital of Miyagi Prefecture and has a high population density near the 2011 Tohoku mainshock. The Fukushima II NPP site is located at 2 km northeast of the Fukushima Daini NPP and 10 km south of the Fukushima Daiichi NPP, where the nuclear disaster occurred due to the 2011 Tohoku earthquake and tsunami. Although Tokyo, the capital of Japan with the highest population density in the country, is approximately 400 km away from the epicenter of the 2011 Tohoku mainshock, major subduction and crustal aftershocks could potentially be triggered which would lead to casualties, building and infrastructure damage, and large economic losses.

Comparison of daily observed PGVs with simulated PGVs

To show that the new framework can anticipate the observed time-varying daily hazard rates in Sendai, Fukushima II NPP, and Tokyo, the observed daily PGV rate ≥ 1 cm/s during the first 7 days is shown in **Figure 7**. The closest stations to the target sites are selected and summarized in **Table 1**. The hazard results with V_{s30} = 400 m/s, 400 m/s, and 200 m/s are selected in Sendai, Fukushima II NPP, and Tokyo, respectively, to match the V_{s30} values at the recording stations. From **Figure 7**, the observed PGV ≥ 1 cm/s is in the range between 10th and 90th percentiles of the simulated PGV. However, only the observed PGV on Day 1 in Fukushima II NPP is outside of the percentile range of the simulated PGV in **Figure 7**b. One reason could be the complex earthquake rupture process of the Tohoku mainshock in space; inversion analysis results by Kurahashi and Irikura (2013) indicated that five strong-motion generation areas (SMGAs) of the Tohoku mainshock are not close to the Fukushima II NPP location and thus observed ground motions are not as intense as predicted using the GMPE which is simply as a function of the shortest distance (rupture distance) to the fault plane. Therefore, the simulated PGV is higher than the observed PGVs at Fukushima II NPP on Day 1.

Spatiotemporal aftershock hazard assessment

From the simulations, aftershocks have greater impact on high PGV values (150 cm/s) than the mainshock. The rates of exceeding PGV from 20 cm/s to 200 cm/s due to the simulated mainshock and from aftershocks on Day 1 with V_{s30} = 300 m/s in Sendai are shown in **Figure 8** to assess the relative importance of simulated mainshock and aftershock hazards. To relate PGV values to damage potential, three MMIs are introduced to link with PGV values in **Figure 8** (https://earthquake.usgs.gov/data/shakemap/background.php) with PGV > 31 cm/s (MMI VII), 60 cm/s (MMI VIII), and 116 cm/s (MMI IX). The simulated mainshock dominates the lower hazard levels, but the aftershock rate is larger than the simulated mainshock beyond a PGV of 150 cm/s (MMI IX). This is because the simulated mainshock always strikes the

514 subduction plate interface, at some distance (typically 40-50km in Sendai) to each site.
515 However, crustal aftershocks are occasionally closer and can thus lead to large PGV values.

516 The aftershock hazard rate in Fukushima II NPP is higher than in Sendai, as shown in
517 **Figure 9**a. Fukushima II NPP is closer to the mainshock rupture area than Sendai, thus more
518 aftershocks are likely to occur nearby. The hazard rate in Tokyo on Day 1 is relatively low,
519 because Tokyo is far from the mainshock rupture. This contrasts with the observation that the
520 seismicity in the Kanto region intensified after the 2011 Tohoku mainshock (Nanjo *et al.*,
521 2013). However, Nanjo *et al.* (2013) considered a lower magnitude threshold with **M**≥1 and
522 no event with **M**≥6 is observed in the Kanto region during one year period after the 2011
523 Tohoku mainshock. Considering uncertainty in the estimation, the increased probability of
524 large events of the 2011 Tohoku sequences is insignificant. Moreover, the three largest
525 historical events (1703 **M**8.2 Genroku earthquake, 1854 **M**8.4 Tonankai-Tokai earthquake, and
526 1923 **M**7.9 Kanto earthquake) are thought to dominate the seismic hazard in Tokyo (Stein *et*
527 *al.*, 2006), and 2011 Tohoku-like great earthquakes do not contribute to the seismic hazard of
528 Tokyo based on the hazard disaggregation of the 2017 version probabilistic seismic hazard map
529 from JSHIS.

530 The differences of the aftershock hazard rates for V_{s30} =200 m/s, 300 m/s, and 400m/s
531 from **Figure 9**b illustrate the effect of the site amplification parameter with a reference V_{s30}
532 value (350 m/s) from the GMPE (Morikawa and Fujiwara, 2013). To contrast the rates of
533 exceeding PGV from 20 cm/s to 200 cm/s over different periods, the rates within 1 day, 1 week,
534 1 month, and 1 year in Sendai are shown in **Figure 9**c, whilst the daily rates of exceeding PGV
535 from Day 1 to Day 5 are shown in **Figure 9**d. Depending on the situation, the aftershock hazard
536 rate may be critical for seismic hazard analysis within one week after the mainshock occurred.
537 This is consistent with the results shown in **Figure 4** for the daily seismicity rate, where the
538 seismicity rate for **M**≥5.5 drops significantly in the first 3 days and then decays slowly.

539 Subduction-zone aftershocks contribute more to the total hazard below PGV = 60 cm/s,
540 while crustal aftershock hazard is greater above 60 cm/s in Sendai and Fukushima II NPP. The
541 daily rates of exceeding PGV from 20 cm/s to 200 cm/s in the first 7 days due to crustal and
542 subduction earthquakes are shown in **Figure 10** to investigate the proportions of aftershock
543 hazard rates that are contributed by crustal and subduction earthquakes in Sendai, Fukushima
544 II NPP, and Tokyo. Subduction-zone aftershocks are more numerous than crustal aftershocks,
545 but they are farther from the considered sites. As a result, subduction aftershocks dominate the
546 hazard below 60 cm/s. In Tokyo, the hazard rate from crustal earthquake is small, and the
547 aftershock hazard rates are dominated by subduction aftershocks.
548 In addition, MMI VII (PGV > 31 cm/s), MMI VIII (PGV > 60 cm/s), and MMI IX
549 (PGV > 116 cm/s) are indicated in **Figure 10** to illustrate the hazard contributions by
550 continental crustal and subduction-zone earthquakes. In Sendai and Fukushima II NPP,
551 subduction aftershocks dominate the MMI VII rate as shown in **Figure 10**a and b. Subduction
552 and crustal aftershocks contribute equally to the MMI VIII exceedances during the first week
553 (**Figure 10**a and b), whereas crustal aftershocks generate higher rates of MMI IX.
554 We consider 3 additional sites with 20km interval along the direction of dip vector of
555 the mainshock rupture model starting with Fukushima II NPP to investigate the aftershock rates
556 changing with the distances in **Figure 11**. In **Figure 11** the daily rates of exceeding PGV in 7
557 Days both for crustal and subduction-zone aftershocks gradually decay with distance. The
558 crustal aftershock hazard is higher than subduction aftershock with PGV>40cm/s. This shows
559 that in comparison with the Fukushima II NPP site, the effect of subduction-zone aftershocks
560 on hazard rate is decreased in the 3 inland sites, because the inland sites have longer shortest
561 distances to the subduction plane.
562 To compare the simulated mainshock hazard and the time-dependent aftershock hazard
563 rate from Days 1 to 7, **Figure 12**a and b show the chances of exceeding PGV > 60 cm/s at

Sendai and Fukushima II NPP, respectively, due to the simulated mainshocks and aftershocks (assuming V_{s30} = 300 m/s). **Figure 12**a shows that the probability of PGV > 60 cm/s in Sendai due to the mainshock is 0.152, whereas the chance is 0.036 due to aftershocks on Day 1. This means that the aftershock hazard on Day 1 adds about 23% to the (conditional) hazard from the mainshock in Sendai on that day. We expect this contribution to vary only by a small amount along the Japanese shoreline close to the rupture area. The result for Fukushima II NPP (**Figure 12**b) shows a similar proportion on Day 1 with the mainshock and aftershock contributions of 0.222 and 0.055, respectively.

To investigate the relative contributions from crustal and subduction aftershocks over several days after the mainshock, **Figure 12**a and b also show the daily hazard rates of crustal and subduction earthquakes. The hazard rates with MMI VIII of subduction and crustal aftershocks in Sendai and Fukushima II NPP are indistinguishable. This is because PGV = 60 cm/s corresponds to the point where the two contributions are about equal (see also **Figure 10**).

Comparison of spatiotemporal aftershock hazard rates with conventional long-term hazard rates

A comparison between the long-term hazard rates from JSHIS and unconditional time-dependent hazard rates from the mainshock-aftershock sequence with V_{s30} = 300 m/s is displayed in **Figure 13** for Sendai, Fukushima II NPP, and Tokyo. To make the JSHIS hazard rate and the time-dependent aftershock hazard rate comparable, we compare the unconditional time-dependent daily hazard rates assuming return periods of 300, 600, and 1000 years for the M9 Tohoku-type subduction earthquake with the daily hazard rates based on the long-term hazard map from JSHIS. The return periods of 300, 600, and 1000 are defined from the literature. Kagan and Jackson (2013) suggested a return period of 300-400 years of Tohoku-like event based on the seismic moment-frequency relation. According to the historical tsunami records, JSHIS considered return periods of 400-800 years for the

589 Tohoku-like event. Simons et al. (2011) suggested return periods in the range of 500-1000
590 years based on the slip accumulation.

591 The long-term hazard rate follows a Poisson distribution with 2% in 50 years.
592 Detailed calculations of the JSHIS hazard rate and the unconditional time-dependent
593 aftershock hazard rate are provided in Appendix 2. We show comparisons with the 2010
594 version (before the 2011 Tohoku event) and the latest 2017 version, each at the PGV
595 exceeded with 2% in 50 years. The JSHIS values are computed from all possible earthquakes,
596 including subduction and crustal earthquakes in land and sea areas. The PGV values of the
597 2017 map corresponding to the 2% probability of exceedance in 50 years are 71 cm/s, 94
598 cm/s, and 134 cm/s, with Vs30 = 351 m/s, 351 m/s, and 403 m/s for Sendai, Fukushima II
599 NPP, and Tokyo, respectively, and indicated in **Figure 13** a, c, and e. The values from the
600 2010 map are displayed in **Figure 13** b, d, and f.

601 After the 2011 Tohoku event, the long-term hazard map was updated significantly. The
602 2017 JSHIS map is higher than the time-dependent rate at all sites assuming V_{s30} = 300 m/s, as
603 shown in **Figure 13**a, c, e. In contrast, the aftershock hazards on Day 1 in Sendai and
604 Fukushima II NPP are greater than the 2010 JSHIS hazard level (**Figure 13**b and d) and the
605 time-dependent hazard rate in Sendai is about twice as large. As shown in **Figure 13**f, Tokyo
606 has the lowest aftershock hazard rate among the three sites. Although we are comparing the
607 relative contributions that aftershocks may play, the total hazard (combined long-term and
608 short-term) should be used for decision-making.

609 Conducting the spatial and temporal hazard assessment using the new framework for
610 the region where a potential **M**9 event can occur in future is important. Before the 2011 Tohoku
611 event, the PGV of the 2010 JSHIS hazard map was lower in Fukushima II NPP (47 cm/s) than
612 in Sendai (64 cm/s). However, after the 2011 Tohoku event, the PGV in Fukushima II NPP
613 was increased significantly (94 cm/s) relative to the PGV in Sendai (71 cm/s). It indicates that

for some regions where **M**9 mega-thrust subduction sequences have never been recorded (e.g., Cascadia subduction zone), conducting spatiotemporal seismic hazard and risk assessments is necessary to investigate the difference in comparison with the conventional probabilistic seismic hazard analysis results.

Because of the updated long-term hazard rate for 2% in 50 years based on the 2011 Tohoku sequence, the effects from a **M**9 earthquake (including its aftershock sequence) to buildings that are newly built after 2017 are limited. However, for buildings that were built before the Tohoku sequence, the damage that may be caused by such sequences could be significant. Therefore, time-dependent rates shown in **Figure 12** and **Figure 13** may be useful for decision-making.

To investigate the change of daily aftershock hazard rates before and after the **M**9 Tohoku-type subduction earthquake, the conditional daily hazard rates from triggered aftershocks right after the Tohoku-like mainshock and the unconditional daily hazard rate from triggered aftershocks are shown in **Figure 14**a and b, respectively. The detailed calculations of the conditional and unconditional daily hazard rates are provided in Appendix 1x 2. According to **Figure 14**a, the forecasted daily aftershock hazard rate immediately following the Tohoku-like mainshock is significantly higher than the 2017 version long-term hazard rate in Sendai and gradually decays over time. The conditional daily aftershock hazard rates could take more than 5 years to trend back to the long-term hazard map from JSHIS given V_{s30} = 300 m/s. The daily unconditional daily hazard rate of aftershocks considering the Tohoku-like mainshock with a 600-years return period is increased by 3% of the long-term hazard rate with V_{s30} = 200 m/s on Day 1 in **Figure 14**b.

Seismic Risk Analysis of M9-triggered Aftershock Sequences in Tohoku

The fragility curves of wood-frame houses from Yamaguchi and Yamazaki (2001) are used (1) to conduct the seismic risk analysis of mainshocks and aftershocks, and (2) to investigate the effects of earthquake types on the wood-frame houses in Japan.

The probability of the damage reaching DS1 due to the simulated mainshock and aftershocks on Day 1 are 11% and 3%, respectively, in Sendai. Aftershocks thus contribute about one fifth of the mainshock's damage probability to DS1 for wood-frame houses on Day 1 (ignoring the damage accumulation effects). The temporal changes of the rates of the three damage states in Sendai and Fukushima II NPP are highlighted in **Figure 15**. The daily damage state rates decay rapidly over the first few days, but also display the slow (heavy-tailed) decay characteristics of the ETAS seismicity model (also seen in the daily hazard rates of **Figure 12**).

The seismic risk information in **Figure 15** can be useful for decision-making about post-earthquake building-tagging and inspection prioritization. The number of days after the mainshock occurred should be taken into consideration as a key factor of the short-term seismic risk assessment. From **Figure 15**a and b, the average damage state rates in Sendai and Fukushima II NPP are decreased after Day 5. This suggests that the building may be exposed to significant risk due to mainshock-aftershock sequences in the first 5 days. Different strategies can be used for post-earthquake building inspection, depending on the number of available inspectors and emergency workers. Houses can be inspected immediately after the mainshock, but the inspectors should be informed in advance about the increased hazard. Therefore, the inspectors can take the potential aftershock hazard into account in the following days. If larger aftershocks are triggered, houses that are tagged with DS1 and DS2 need to be assessed once more. Alternatively, the inspection of the houses can take place after Day 5 to make sure the damage potential due to the more likely aftershocks is included.

The damage state rates of wood-frame houses that are caused by crustal and subduction aftershock hazards are shown in **Figure 16**. Crustal and subduction earthquakes induce about the same DS1 rates. The DS2 and DS3 rates, however, are dominated by crustal earthquakes in Sendai and Fukushima II NPP. The median values of the fragility curves for DS1, DS2, and DS3 are 77 cm/s, 105 cm/s, and 141 cm/s, respectively. Experiencing a PGV = 60 cm/s, which corresponds to the value of intersection between the subduction aftershock and crustal aftershock in **Figure 10**, could result in DS1 for the wood-frame houses, whereas DS2 and DS3 require a PGV higher than 60 cm/s, which are mainly contributed from large crustal earthquakes. This suggests that crustal aftershocks could cause more significant damage than the subduction aftershocks for wood-frame houses in Japan. The decision-making for wood-frame houses in post-earthquake risk assessments described above is an example of how the time-dependent hazard rate can be implemented for risk analyses. In general, the daily hazard rates in **Figure 12** can be widely applied for different types of buildings and infrastructures.

Conclusions

This study investigated the importance of subduction and crustal aftershocks triggered by a **M**9 mega-thrust subduction event in spatiotemporal seismic hazard and risk assessments. The developed framework includes a seismicity model, hazard analysis, and risk analysis. Specifically, we convolved the ETAS model with a GMPE and fragility model to conduct the hazard and risk analyses. To model the **M**9 mega-thrust subduction sequences in space, we proposed a new spatial distribution of the first-generation aftershocks by combining the latest scaling law of rupture area with a power law decay beyond the main rupture area. By using this new spatial distribution, good agreement is achieved between the observed 2011 Tohoku sequence and the simulated daily seismicity rates with **M**≥5.5 and PGV rates ≥ 1 cm/s. We

685 estimated how much simulated aftershock hazards add to simulated mainshock hazards
686 considering uncertainties of the seismicity model, GMPEs, and fragility curves.
687 The results showed that:
688 • Aftershocks on Day 1 at the onshore sites that are close to the mainshock rupture area
689 (e.g., Sendai and Fukushima II NPP in this study) could have a higher impact on high
690 PGV values > 150 cm/s than the simulated mainshock, due to occasional crustal
691 aftershocks.
692 • The aftershock hazard rate in Fukushima II NPP is higher than in Sendai, because
693 Fukushima II NPP is closer to the mainshock rupture plane than Sendai.
694 • According to our model, a **M**9 2011 Tohoku-like earthquake sequence does not have
695 significant impact on JSHIS's estimate for Tokyo, which is dominated by presumed
696 recurrences of the 1703 **M**8.2 Genroku earthquake, the 1854 **M**8.4 Tonankai-Tokai
697 earthquake, and the 1923 **M**7.9 Kanto earthquake.
698 • Triggered subduction earthquakes are more numerous than crustal counterparts with
699 **M**5.5, but the crustal aftershocks contribute greater hazard above PGV = 60 cm/s (MMI
700 VIII) and V_{s30} = 300 m/s than the subduction aftershocks. Therefore, the subduction
701 aftershocks have a significant impact on MMI VII, whereas the crustal earthquakes
702 contribute more to MMI IX and beyond.
703 • The aftershock hazard rate contributes about 23% of the PGV rate on Day 1 in Sendai.
704 Fukushima II NPP shows a similar proportion on Day 1, but the mainshock and
705 aftershock rates are higher than Sendai by a factor of 1.5.
706 • The daily hazard rate from aftershocks alone exceeds the 2010 long-term (total) hazard
707 level from the JSHIS (which considers all earthquakes) on Day 1 in Sendai and
708 Fukushima II NPP. The daily aftershock hazard rate immediately after the mainshock

709 is significantly high and could take more than 5 years to trend back to the 2017 JSHIS
710 long-term hazard map in Sendai.
711 • Assuming V_{s30} = 300 m/s, the simulated mainshock and aftershocks contribute
712 approximately 80% and 20% to the total DS1 rate at Sendai and Fukushima II NPP on
713 Day 1, and the mean damage state rate gradually decreases from Day 2 to 5. This may
714 be useful for prioritizing building inspection. Wood-frame houses in Sendai and
715 Fukushima II NPP can be inspected by a structural engineer after Day 5.
716 • Crustal aftershocks have a higher probability to damage the wood-frame houses than
717 the subduction earthquakes in Sendai and Fukushima II NPP.

718 The developed procedure to assess the spatiotemporal seismic hazard analysis with the
719 ETAS model and GMPEs is generic and can be applied to other regions with **M**8.5+ subduction
720 earthquakes. However, the mainshock source parameters (e.g., epicenter, rupture length and
721 width, and strike and dip angles) are necessary as inputs for the ETAS simulation. Ignoring the
722 observed M9 sequence (e.g., the 2011 Tohoku event) would increase the uncertainty of the
723 hazard rates. Therefore, if the mainshock source parameters are available immediately after the
724 mainshock, forecasting aftershocks associated with quasi-real time hazard assessments would
725 be applicable. The output of the short-term hazard and risk results may be particularly
726 beneficial for short-term decision-making within the first 7 days after the mainshock. For the
727 regions without observed M9-class events, different mainshock rupture scenarios should be
728 discussed under the new simulation framework.

729 Local conditions (e.g., stress fields or volcanic zones) of the inland area could be
730 considered to the future study of the distant aftershock triggering. Several studies have shown
731 that static and dynamic stress changes (Ishibe *et al.*, 2011; Toda *et al.*, 2011; Kato *et al.*, 2013)
732 are necessary to consider for distant aftershocks. According to the 2011 Tohoku sequence,
733 distance is not the only factor that controls the aftershock rates in the far field. Local stress

fields could be examined before the mega-thrust event for such long-distance aftershock triggering (Imanishi *et al.*, 2012). In addition, Hirose *et al.* (2011) also indicate seismicity rate tend to be increased in the volcanic regions after the rupture of major active fault.

Data and Resources

The JMA catalog is from http://www.data.jma.go.jp/svd/eqev/data/bulletin/hypo_e.html. (last accessed on January 20, 2017). The ANSS catalog is from http://www.quake.geo.berkeley.edu/anss/catalog-search.html (last accessed on March 15, 2017). The gCMT catalog is from http://www.globalcmt.org/CMTsearch.html (last accessed on March 15, 2017). The ISC catalog is from http://www.isc.ac.uk/iscbulletin/search/catalogue/ (last accessed on March 15, 2017). The Vs30 information is from http://www.j-shis.bosai.go.jp/en/ (last accessed on June 20, 2017). The ground motion records are from the K-NET and KiK-net (http://www.kyoshin.bosai.go.jp/) and the SK-net (http://www.sknet.eri.u-tokyo.ac.jp/) (last accessed on June 02, 2015).

Acknowledgements

The authors gratefully acknowledge financial support from the Leverhulme Trust (RPG-2017-006) for the GENESIS (Global Earthquake Resilience for Natural-Engineering-Social Interacting Systems) project. The authors appreciate support from the Southern California Earthquake Center.

References

Abrahamson, N., W. Silva, and R. Kamai (2014) Summary of the ASK14 ground motion relation for active crustal regions, *Earthq. Spectra* **30**, 1025–1055.

759 Abrahamson, N., N. Gregor, and K. Addo (2016) BC Hydro ground motion prediction
760 equations for subduction earthquakes, *Earthq. Spectra* **32**, 23–44.
761 Aki, K. (1965) Maximum likelihood estimate of b in the formula log N= a-bM and its
762 confidence limits, *Bull. Earthq. Res. Inst., Tokyo Univ.* **43**, 237–239.
763 Amorèse, D. (2007) Applying a change-point detection method on frequency-magnitude
764 distributions, *Bull. Seismol. Soc. Am.* **97**, 1742–1749.
765 Asano, K. and T. Iwata (2011) Characterization of stress drops on asperities estimated from
766 the heterogeneous kinematic slip model for strong motion prediction for inland crustal
767 earthquakes in Japan, *Pure Appl. Geophys.* **168**, 105–116.
768 Asano, Y., T. Saito, Y. Ito, K. Shiomi, H. Hirose, T. Matsumoto, S. Aoi, S. Hori, and S.
769 Sekiguchi (2011) Spatial distribution and focal mechanisms of aftershocks of the 2011
770 off the Pacific coast of Tohoku Earthquake, *Earth, Planets Sp.* **63**, 669–673.
771 Boyd, O.S. (2012) Including foreshocks and aftershocks in time-independent probabilistic
772 seismic-hazard analyses, *Bull. Seismol. Soc. Am.* **102**, 909–917.
773 Das, S. and C. Henry (2003) Spatial relation between main earthquake slip and its aftershock
774 distribution, *Rev. Geophys.* **41**.
775 Felzer, K.R. and E.E. Brodsky (2006) Decay of aftershock density with distance indicates
776 triggering by dynamic stress, *Nature* **441**, 735–738.
777 Field, E., K. Milner, J. Hardebeck, M. Page, N. van der Elst, T.H. Jordan, A.J. Michael, B.E.
778 Shaw, and M.J. Werner (2017a) A spatiotemporal clustering model for the third
779 Uniform California Earthquake Rupture Forecast (UCERF3-ETAS): toward an
780 operational earthquake forecast, *Bull. Seismol. Soc. Am.* **107**, 1049–1081.
781 Field, E., K. Porter, and K. Milner (2017b) A prototype operational earthquake loss model for
782 California based on UCERF3-ETAS--a first look at valuation, *Earthq. Spectra* **33**,
783 1279–1299, doi: 10.1193/011817EQS017M.

784 Fukushima, Y., Y. Takada, and M. Hashimoto (2013) Complex ruptures of the 11 April 2011
785 Mw 6.6 Iwaki earthquake triggered by the 11 March 2011 Mw 9.0 Tohoku earthquake,
786 Japan, *Bull. Seismol. Soc. Am.* **103**, 1572–1583.
787 Gerstenberger, M., G. McVerry, D. Rhoades, and M. Stirling (2014) Seismic hazard
788 modeling for the recovery of Christchurch, *Earthq. Spectra* **30**, 17–29.
789 Goda, K., F. Wenzel, and R. De Risi (2015) Empirical assessment of non-linear seismic
790 demand of mainshock-aftershock ground-motion sequences for Japanese earthquakes,
791 *Front. Built Environ.* **1**, 6, doi: 10.3389/fbuil.2015.00006.
792 Goda, K., T. Yasuda, N. Mori, and T. Maruyama (2016) New scaling relationships of
793 earthquake source parameters for stochastic tsunami simulation, *Coast. Eng. J.* **58**,
794 1650010–1–1650010–40, doi: 10.1142/S0578563416500108.
795 Hainzl, S., J. Moradpour, and J. Davidsen (2014) Static stress triggering explains the
796 empirical aftershock distance decay, *Geophys. Res. Lett.* **41**, 8818–8824.
797 Hainzl, S., O. Zakharova, and D. Marsan (2013) Impact of aseismic transients on the
798 estimation of aftershock productivity parameters, *Bull. Seismol. Soc. Am.* **103**, 1723–
799 1732.
800 Harte, D.S. (2015) Model parameter estimation bias induced by earthquake magnitude cut-
801 off, *Geophys. J. Int.* **204**, 1266–1287.
802 Hayes, G.P., D.J. Wald, and R.L. Johnson (2012) Slab1.0: a three-dimensional model of
803 global subduction zone geometries, *J. Geophys. Res. Solid Earth* **117**.
804 Helmstetter, A., Y.Y. Kagan, and D.D. Jackson (2005) Importance of small earthquakes for
805 stress transfers and earthquake triggering, *J. Geophys. Res. Solid Earth* **110**, doi:
806 10.1029/2004JB003286.
807 Hirose, F., K. Miyaoka, N. Hayashimoto, T. Yamazaki, and M. Nakamura (2011) Outline of
808 the 2011 off the Pacific coast of Tohoku earthquake (Mw 9.0)—seismicity: foreshocks,

809 mainshock, aftershocks, and induced activity—, *Earth, planets Sp.* **63**, 1.
810 Iervolino, I., E. Chioccarelli, M. Giorgio, W. Marzocchi, G. Zuccaro, M. Dolce, and G.
811 Manfredi (2015) Operational (short-term) earthquake loss forecasting in Italy, *Bull.*
812 *Seismol. Soc. Am.* **105**, 2286–2298.
813 Imanishi, K., R. Ando, and Y. Kuwahara (2012) Unusual shallow normal-faulting earthquake
814 sequence in compressional northeast Japan activated after the 2011 off the Pacific coast
815 of Tohoku earthquake, *Geophys. Res. Lett.* **39**, doi: 10.1029/2012GL051491.
816 Ishibe, T., K. Shimazaki, K. Satake, and H. Tsuruoka (2011) Change in seismicity beneath
817 the Tokyo metropolitan area due to the 2011 off the Pacific coast of Tohoku Earthquake,
818 *Earth, planets Sp.* **63**, 731–735.
819 Jordan, T.H., Y.T. Chen, P. Gasparini, R. Madariaga, I. Main, W. Marzocchi, G.
820 Papadopoulos, G. Sobolev, K. Yamaoka, and J. Zschau (2011) Operational earthquake
821 forecasting: state of knowledge and guidelines for utilization, *Ann. Geophys.* **54**, 319–
822 391.
823 Jordan, T.H. and L.M. Jones (2010) Operational earthquake forecasting: some thoughts on
824 why and how, *Seismol. Res. Lett.* **81**, 571–574.
825 Kagan, Y.Y. and D.D. Jackson (1994) Long-term probabilistic forecasting of earthquakes, *J.*
826 *Geophys. Res. Solid Earth* **99**, 13685–13700.
827 Kagan, Y.Y. and L. Knopoff (1987) Statistical short-term earthquake prediction, *Science.*
828 **236**, 1563–1567.
829 Kanaori, Y., S. Kawakami, and K. Yairi (1991) Space-time distribution patterns of
830 destructive earthquakes in the inner belt of central Japan: activity intervals and locations
831 of earthquakes, *Eng. Geol.* **31**, 209–230.
832 Kato, A., J. Fukuda, and K. Obara (2013) Response of seismicity to static and dynamic stress
833 changes induced by the 2011 M9. 0 Tohoku-Oki earthquake, *Geophys. Res. Lett.* **40**,

834 3572–3578.
835 Koketsu, K., Y. Yokota, N. Nishimura, Y. Yagi, S. Miyazaki, K. Satake, Y. Fujii, H. Miyake,
836 S. Sakai, Y. Yamanaka, and T. Okada (2011) A unified source model for the 2011
837 Tohoku earthquake, *Earth Planet. Sci. Lett.* **310**, 480–487.
838 Kurahashi, S. and K. Irikura (2013) Short-period source model of the 2011 Mw 9.0 off the
839 Pacific coast of Tohoku earthquake, *Bull. Seismol. Soc. Am.* **103**, 1373–1393.
840 Lombardi, A.M. and W. Marzocchi (2010) The ETAS model for daily forecasting of Italian
841 seismicity in the CSEP experiment, *Ann. Geophys.*
842 Marzocchi, W., A.M. Lombardi, and E. Casarotti (2014) The establishment of an operational
843 earthquake forecasting system in Italy, *Seismol. Res. Lett.* **85**, 961–969.
844 Marzocchi, W. and M. Taroni (2014) Some thoughts on declustering in probabilistic seismic-
845 hazard analysis, *Bull. Seismol. Soc. Am.* **104**, 1838–1845.
846 McGuire, R.K. (2004) *Seismic hazard and risk analysis*, EERI Monograph MNO-10,
847 Earthquake Engineeering Research Institute, Oakland, California.
848 Midorikawa, S., Y. Ito, and H. Miura (2011) Vulnerability functions of buildings based on
849 damage survey data of earthquakes after the 1995 Kobe earthquake, *J. Japan Assoc.*
850 *Earthq. Eng.* **11**, 34–47.
851 Miura, S., Y. Suwa, T. Sato, K. Tachibana, and A. Hasegawa (2004) Slip distribution of the
852 2003 northern Miyagi earthquake (M6.4) deduced from geodetic inversion, *Earth,*
853 *planets Sp.* **56**, 95–101.
854 Morikawa, N. and H. Fujiwara (2013) A new ground motion prediction equation for Japan
855 applicable up to M9 mega-earthquake, *J. Disaster Res.* **8**, 878–888.
856 Nakahara, H., T. Nishimura, H. Sato, M. Ohtake, S. Kinoshita, and H. Hamaguchi (2002)
857 Broadband source process of the 1998 Iwate prefecture, Japan, earthquake as revealed
858 from inversion analyses of seismic waveforms and envelopes, *Bull. Seismol. Soc. Am.*

92, 1708–1720.

Nanjo, K.Z., T. Ishibe, H. Tsuruoka, D. Schorlemmer, Y. Ishigaki, and N. Hirata (2010) Analysis of the completeness magnitude and seismic network coverage of Japan, *Bull. Seismol. Soc. Am.* **100**, 3261–3268.

Nanjo, K.Z., S. Sakai, A. Kato, H. Tsuruoka, and N. Hirata (2013) Time-dependent earthquake probability calculations for southern Kanto after the 2011 M9.0 Tohoku earthquake, *Geophys. J. Int.* **193**, 914–919.

Ogata, Y. (1998) Space-time point-process models for earthquake occurrences, *Ann. Inst. Stat. Math.* **50**, 379–402.

Ogata, Y. (1988) Statistical models for earthquake occurrences and residual analysis for point processes, *J. Am. Stat. Assoc.* **83**, 9–27.

Ogata, Y. and J. Zhuang (2006) Space-time ETAS models and an improved extension, *Tectonophysics* **413**, 13–23.

Ramanna, C.K. and G.R. Dodagoudar (2012) Seismic hazard analysis using the adaptive Kernel density estimation technique for Chennai City, *Pure Appl. Geophys.* **169**, 55–69.

Rietbrock, A., I. Ryder, G. Hayes, C. Haberland, D. Comte, S. Roecker, and H. Lyon-Caen (2012) Aftershock seismicity of the 2010 Maule Mw=8.8, Chile, earthquake: correlation between co-seismic slip models and aftershock distribution?, *Geophys. Res. Lett.* **39**, doi: 10.1029/2012GL051308.

Scordilis, E.M. (2005) Globally valid relations converting Ms, mb and MJMA to Mw, In: *Meeting on Earthquake Monitoring and Seismic Hazard Mitigation in Balkan Countries, NATO ARW, Borovetz, Bulgaria*, 11–17.

Seif, S., A. Mignan, J.D. Zechar, M.J. Werner, and S. Wiemer (2017) Estimating ETAS: the effects of truncation, missing data, and model assumptions, *J. Geophys. Res. Solid Earth* **122**, 449–469.

884 Shao, G., X. Li, C. Ji, and T. Maeda (2011) Focal mechanism and slip history of the 2011
885 Mw 9.1 off the Pacific coast of Tohoku earthquake, constrained with teleseismic body
886 and surface waves, *Earth, Planets Sp.* **63**, 564.
887 Shi, Y. and B.A. Bolt (1982) The standard error of the magnitude-frequency b value, *Bull.*
888 *Seismol. Soc. Am.* **72**, 1677–1687.
889 Stein, R.S., S. Toda, T. Parsons, and E. Grunewald (2006) A new probabilistic seismic hazard
890 assessment for greater Tokyo, *Philos. Trans. R. Soc. London A Math. Phys. Eng. Sci.*
891 **364**, 1965–1988.
892 Suárez, G., V. García-Acosta, and R. Gaulon (1994) Active crustal deformation in the Jalisco
893 block, Mexico: evidence for a great historical earthquake in the 16th century,
894 *Tectonophysics* **234**, 117–127.
895 Suzuki, W., S. Aoi, H. Sekiguchi, and T. Kunugi (2011) Rupture process of the 2011
896 Tohoku-Oki mega-thrust earthquake (M9. 0) inverted from strong-motion data,
897 *Geophys. Res. Lett.* **38**, doi: 10.1029/2011GL049136.
898 Thingbaijam, K.K.S., P. Martin Mai, and K. Goda (2017) New empirical earthquake-source
899 scaling laws, *Bull. Seismol. Soc. Am.* **107**, 2225–2246.
900 Toda, S., R.S. Stein, and J. Lin (2011) Widespread seismicity excitation throughout central
901 Japan following the 2011 M=9.0 Tohoku earthquake and its interpretation by coulomb
902 stress transfer, *Geophys. Res. Lett.* **38**, doi: 10.1029/2011GL047834.
903 Toda, S. and H. Tsutsumi (2013) Simultaneous reactivation of two, subparallel, inland
904 normal faults during the Mw 6.6 11 April 2011 Iwaki earthquake triggered by the Mw
905 9.0 Tohoku-oki, Japan, earthquake, *Bull. Seismol. Soc. Am.* **103**, 1584–1602.
906 Toro, G.R. and W.J. Silva (2001) Scenario earthquakes for Saint Louis, MO, Memphis, TN,
907 and seismic hazard maps for the central United States region: including the effect of site
908 conditions: Technical report to U.S. Geological Survey, Reston, Virginia, under

Contract 1434-HQ-97-GR-02981, available at //http://www.uta.edu/faculty/mattioli/research/nmsz/nmsz_risk_report.pdf (last accessed June 2018).

Vere-Jones, D. (1992) Statistical methods for the description and display of earthquake catalogs, in *Statistics in the environmental and Earth sciences*, A. T. Walden and P Guttorp (Editors), Arnold Publishers, London, 220–246.

Wang, Q., D.D. Jackson, and Y.Y. Kagan (2011) California earthquake forecasts based on smoothed seismicity: Model choices, *Bull. Seismol. Soc. Am.* **101**, 1422–1430.

Wang, Q., D.D. Jackson, and J. Zhuang (2010) Missing links in earthquake clustering models, *Geophys. Res. Lett.* **37**, doi: 10.1029/2010GL044858.

Wells, D.L. and K.J. Coppersmith (1994) New empirical relationships among magnitude, rupture length, rupture width, rupture area, and surface displacement, *Bull. Seismol. Soc. Am.* **84**, 974–1002.

Werner, M.J., A. Helmstetter, D.D. Jackson, and Y.Y. Kagan (2011) High-resolution long-term and short-term earthquake forecasts for California, *Bull. Seismol. Soc. Am.* **101**, 1630–1648.

Woo, G. (1996) Kernel estimation methods for seismic hazard area source modeling, *Bull. Seismol. Soc. Am.* **86**, 353–362.

Wu, H., K. Masaki, K. Irikura, and S. Kurahashi (2016) Empirical fragility curves of buildings in northern Miyagi Prefecture during the 2011 off the Pacific coast of Tohoku earthquake, *J. Disaster Res.* **11**, 1253–1270.

Yaghmaei-Sabegh, S., P. Shoaeifar, and N. Shoaeifar (2017) Probabilistic seismic-hazard analysis including earthquake clusters, *Bull. Seismol. Soc. Am.* **107**, 2367–2379.

Yagi, Y. and Y. Fukahata (2011) Rupture process of the 2011 Tohoku-Oki earthquake and absolute elastic strain release, *Geophys. Res. Lett.* **38**, doi: 10.1029/2011GL048701.

934 Yamaguchi, N. and F. Yamazaki (2001) Estimation of strong motion distribution in the 1995
935 Kobe earthquake based on building damage data, *Earthq. Eng. Struct. Dyn.* **30**, 787–
936 801.
937 Yeo, G.L. and C.A. Cornell (2009) A probabilistic framework for quantification of aftershock
938 ground-motion hazard in California: methodology and parametric study, *Earthq. Eng.*
939 *Struct. Dyn.* **38**, 45–60.
940 Youngs, R.R., N. Abrahamson, F.I. Makdisi, and K. Sadigh (1995) Magnitude-dependent
941 variance of peak ground acceleration, *Bull. Seismol. Soc. Am.* **85**, 1161–1176.
942 Zhao, J.X., J. Zhang, A. Asano, Y. Ohno, T. Oouchi, T. Takahashi, H. Ogawa, K. Irikura,
943 H.K. Thio, P.G. Somerville, Y. Fukushima, and Y. Fukushima (2006) Attenuation
944 relations of strong ground motion in Japan using site classification based on
945 predominant period, *Bull. Seismol. Soc. Am.* **96**, 898–913.
946 Zhuang, J. (2011) Next-day earthquake forecasts for the Japan region generated by the ETAS
947 model, *Earth Planets Sp.* **63**, 207–216.
948 Zhuang, J., Y. Ogata, and D. Vere-Jones (2004) Analyzing earthquake clustering features by
949 using stochastic reconstruction, *J. Geophys. Res. Solid Earth* **109**, doi:
950 10.1029/2003JB002879.
951

952 ## Full mailing address for each author

953 Lizhong Zhang: lz0560@bristol.ac.uk
954 Maximilian J. Werner: max.werner@bristol.ac.uk
955 Katsuichiro Goda: katsu.goda@bristol.ac.uk

Tables

Table 1: Selected record stations for PGV comparisons

Location	Record station name	Number of records	Distance to the target site (km)	V_{s30} (m/s)
Sendai	MYG012	305	1.4	436
Fukushima II NPP	FKS010	555	10.0	430
Tokyo	EKO.ERI	85	0.9	266

Table 2: Temporal windows and M_{cut} for ETAS parameter estimation

Cases	Auxiliary window	Target window	M_{cut}	Fixed parameters
1	1970.01.01-1980.01.01	1980.01.01-2015.12.31	4.7	NA
2	2008.03.11-2011.03.10	2011.03.11-2015.03.11	4.7	NA
3	1970.01.01-1980.01.01	1980.01.01-2015.12.31	4.7	α

Table 3: ETAS parameter estimation results (standard errors are shown in parentheses).

Cases	K_0 (event/day)	α (magnitude^{-1})	c (day)	p	d (km^2)	γ (magnitude^{-1})	q
1	0.1770 (0.0110)	1.78 (0.033)	0.0215 (0.0030)	1.16 (0.013)	13.37 (2.26)	1.69 (0.044)	2.12 (0.13)
2	0.1846 (0.0170)	1.72 (0.048)	0.0492 (0.0098)	1.28 (0.026)	13.32 (3.83)	1.68 (0.063)	1.96 (0.21)
3	0.0640 (0.0021)	2.3 (fixed) (0)	0.0281 (0.0040)	1.18 (0.014)	6.89 (1.40)	2.04 (0.042)	2.13 (0.14)
4	0.0640 (0.0021)	2.3 (fixed) (0)	0.0215 (0.0030)	1.16 (0.013)	13.37 (2.26)	1.69 (0.044)	2.12 (0.13)

List of figure captions

Figure 1. Framework for spatiotemporal seismic hazard and risk assessment.

Figure 2. An example of the spatial probability density function of the first generation of aftershocks outside a simulated rupture area (500 km×300 km). We employ 1D and 2D kernel power-laws for aftershocks outside the rupture area, respectively.

Figure 3: (a) Target (dotted line) and data (dashed line) windows for ETAS parameter estimation. Stars denote the three locations chosen to illustrate the hazard and risk calculations: Sendai (141.0286ºE, 38.3072ºN), Fukushima II NPP (141.0132ºE, 37.3236ºN), and Tokyo (139.7679ºE, 35.7235ºN). (b) Magnitude of completeness of the JMA catalog from 1970 to 2015 using a sliding time window of 200 events in the target window. (c) Observed magnitude-frequency distributions and fitted Gutenberg-Richter laws with maximum likelihood estimates of the *b-values* and 5%-95% percentiles. (d) Observed 2D aftershock histogram with **M**≥5.5 during the 100 days after the 2011 Tohoku mainshock.

Figure 4. Comparison of observed and simulated aftershocks with **M**≥5.5 after the 2011 Tohoku earthquake: (a) Magnitude frequency distribution in the first 100 days and 95% uncertainty range from the simulations in square root scale. (b) Daily number of events in the first 30 days with 95% uncertainty range.

Figure 5. Two ETAS simulations in comparison with the 2011 Tohoku events with **M**≥5.5. (a, c) Simulated 2D aftershock histograms during the first 100 days. (b, d) Comparison of daily numbers of observed and simulated aftershocks. The mainshock source parameters

997 (epicenter, slip angle, strike angle, rupture length, and rupture width) are randomly generated
998 from the empirical distributions.
999
1000 **Figure 6.** (a) Median values of PGV with *Vs30* = 300 m/s for subduction earthquakes from
1001 **M6-M9** using the GMPE by Morikawa and Fujiwara (2013). (b) Median values of PGV with
1002 *Vs30* = 300 m/s for crustal earthquakes from **M5-M8** using the GMPE by Morikawa and
1003 Fujiwara (2013). (c) Fragility curves (the probability of damage states against PGV) of wood-
1004 frame houses for Japan with slight damage, moderate damage, and heavy damage.
1005
1006 **Figure 7.** Comparison of mean simulated and observed rate of PGV > 1 cm/s per day during
1007 the first 7 days after the 2011 Tohoku mainshock in (a) Sendai, (b) Fukushima II NPP and (c)
1008 Tokyo. Vertical bars denote 10th to 90th percentile range of simulated ground motions.
1009
1010 **Figure 8.** Rates of exceeding aftershock PGVs on left y-axis (diamond) on Day 1 in Sendai
1011 in comparison with PGV rates of simulated mainshock on right y-axis (upward-pointing
1012 triangle).
1013
1014 **Figure 9.** (a) Rates of exceeding aftershock PGVs (diamond) on Day 1 in Sendai in
1015 comparison with Fukushima II NPP (square), and Tokyo (star). (b) Three soil conditions with
1016 *Vs30* = 200 m/s (circle with dashed line), 300 m/s (diamond), and 400 m/s (circle with dotted
1017 line). (c) time periods with T = 1 day (diamond), 1week (circle), 1 month (right-pointing
1018 triangle), and 1 year (star). (d) Day 1 (diamond), Day 2 (upward-pointing triangle), Day 3
1019 (pentagram), Day 4 (downward-pointing triangle), and Day 5(square).
1020

Figure 10. Daily rates of exceeding PGV for crustal and subduction aftershocks (circles with solid line), crustal (upward-pointing triangles with dashed line) and subduction (squares with dotted line) aftershocks in the first 7 days in (a) Sendai, (b) Fukushima II NPP, and (c) Tokyo.

Figure 11. Daily rates of exceeding PGV for crustal and subduction aftershocks in the first 7 days 20km, 40km, and 60km away from Fukushima II NPP.

Figure 12. Daily hazard rates of PGV > 60 cm/s due to crustal and subduction aftershocks in comparison with simulated mainshock (stars) in (a) Sendai and (b) Fukushima II NPP.

Figure 13. Left panels: comparison between daily time-dependent hazard rate (squares) and the 2017 JSHIS long-term hazard rate corresponding to 2% in 50 years (dash-dotted line) in (a) Sendai, (c) Fukushima II NPP, and (e) Tokyo. Panels in right column: corresponding comparisons with the 2010 JSHIS rate.

Figure 14. (a) Decay of conditional aftershock hazard rates in Sendai immediately after the Tohoku-like mainshock in one year. (b) Decay of unconditional aftershock hazard rates considering a 600-years return period of the Tohoku-like mainshock.

Figure 15. Comparison of mean daily DS rates of simulated mainshock and aftershocks in (a) Sendai and (b) Fukushima II NPP.

Figure 16. Mean daily damage state rates of crustal and subduction aftershocks for DS1, DS 2 and DS3 in (a) Sendai and (b) Fukushima II NPP.

1046

1047

1048

Figures

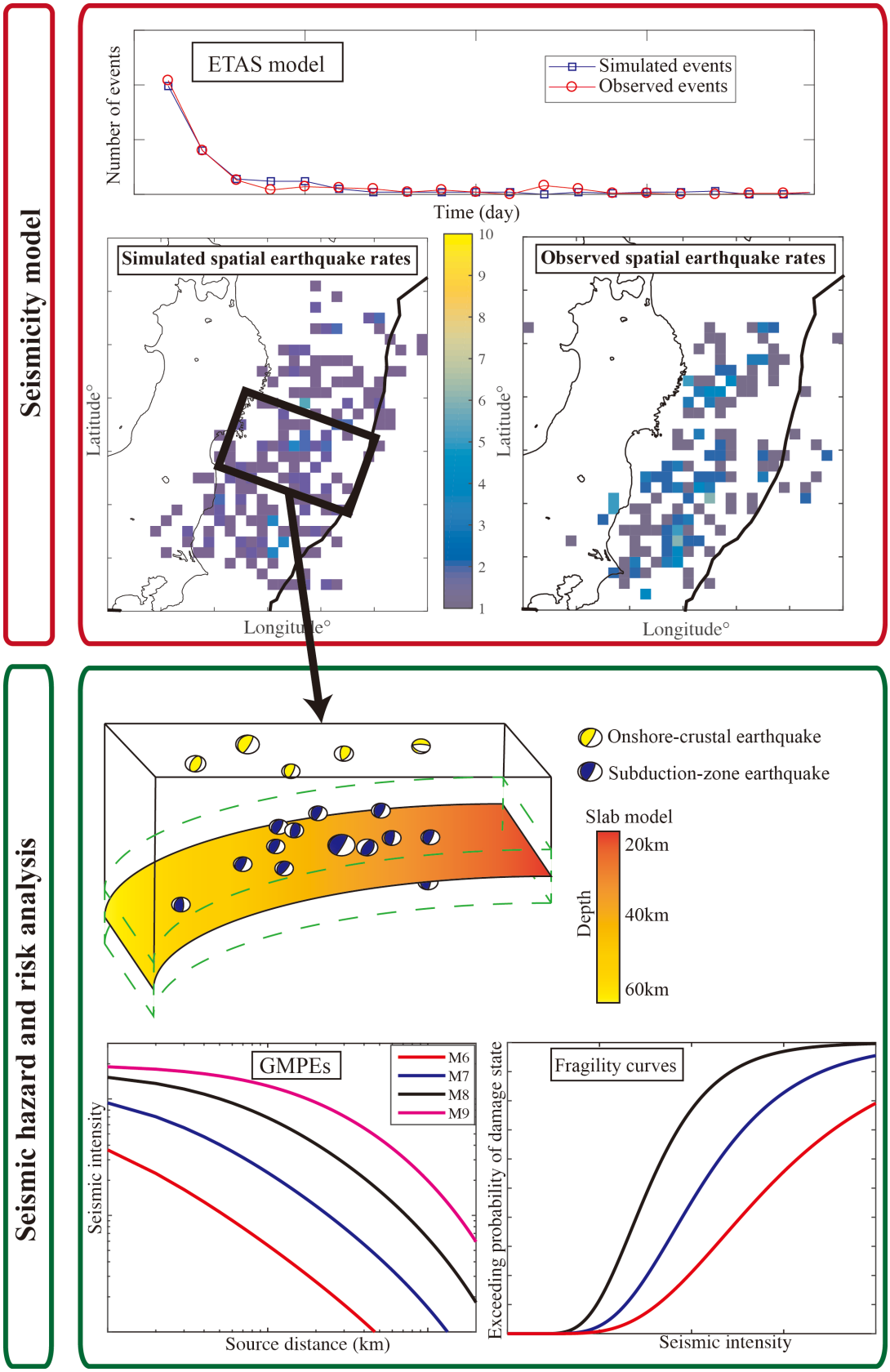

Figure 1. Framework for spatiotemporal seismic hazard and risk assessment.

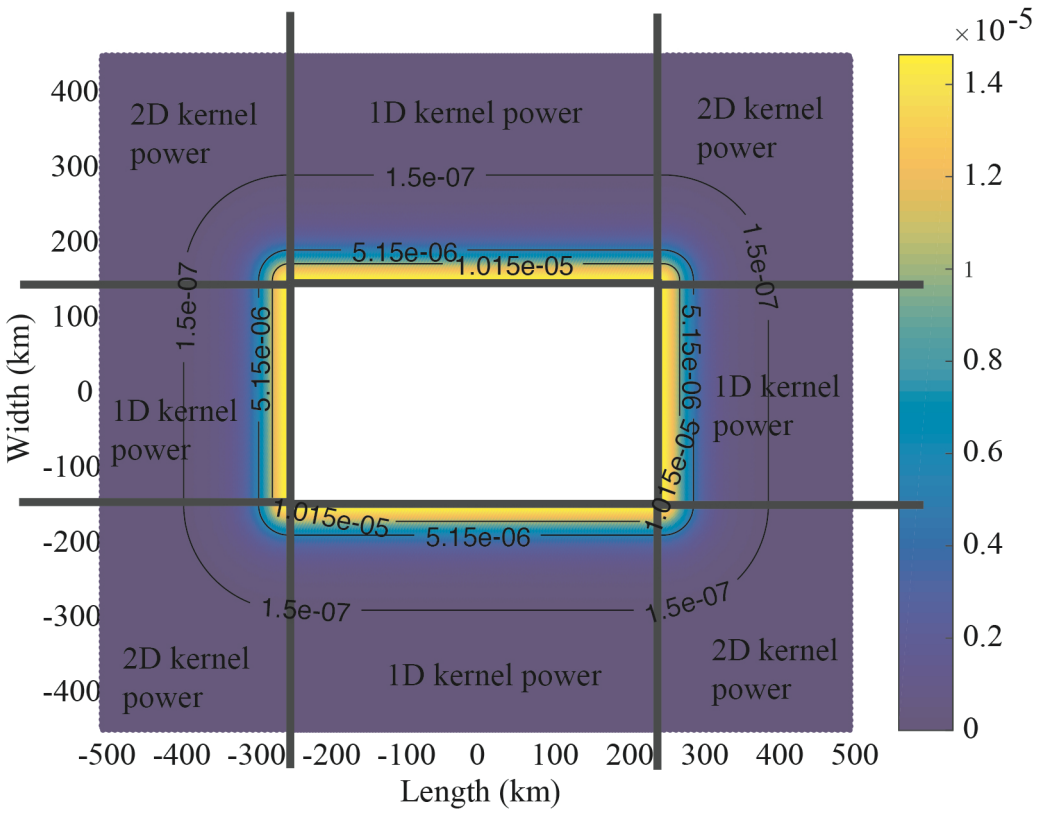

Figure 2. An example of the spatial probability density function of the first generation of aftershocks outside a simulated rupture area (500 km×300 km). We employ 1D and 2D kernel power-laws for aftershocks outside the rupture area, respectively.

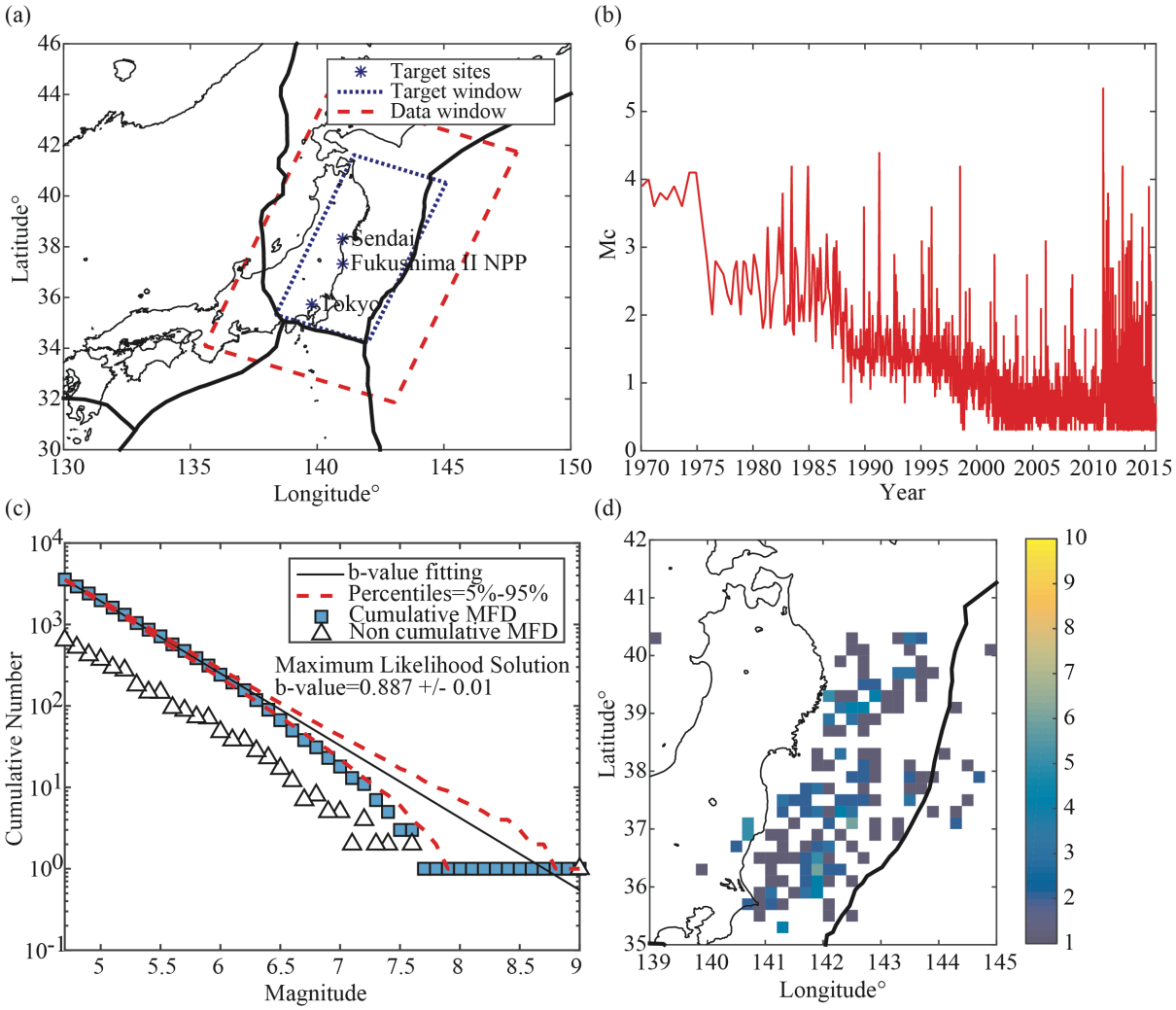

1062

1063 **Figure 3:** (a) Target (dotted line) and data (dashed line) windows for ETAS parameter
1064 estimation. Stars denote the three locations chosen to illustrate the hazard and risk calculations:
1065 Sendai (141.0286ºE, 38.3072ºN), Fukushima II NPP (141.0132ºE, 37.3236ºN), and Tokyo
1066 (139.7679ºE, 35.7235ºN). (b) Magnitude of completeness of the JMA catalog from 1970 to
1067 2015 using a sliding time window of 200 events in the target window. (c) Observed magnitude-
1068 frequency distributions and fitted Gutenberg-Richter laws with maximum likelihood estimates
1069 of the *b*-values and 5%-95% percentiles. (d) Observed 2D aftershock histogram with **M**≥5.5
1070 during the 100 days after the 2011 Tohoku mainshock.

1071

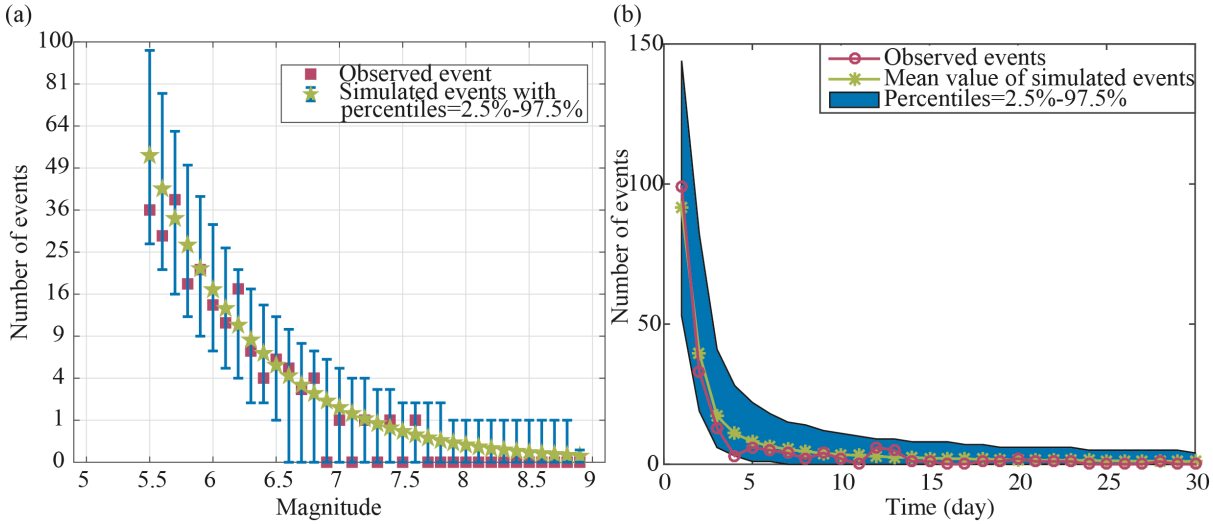

Figure 4. Comparison of observed and simulated aftershocks with **M**≥5.5 after the 2011 Tohoku earthquake: (a) Magnitude frequency distribution in the first 100 days and 95% uncertainty range from the simulations in square root scale. (b) Daily number of events in the first 30 days with 95% uncertainty range.

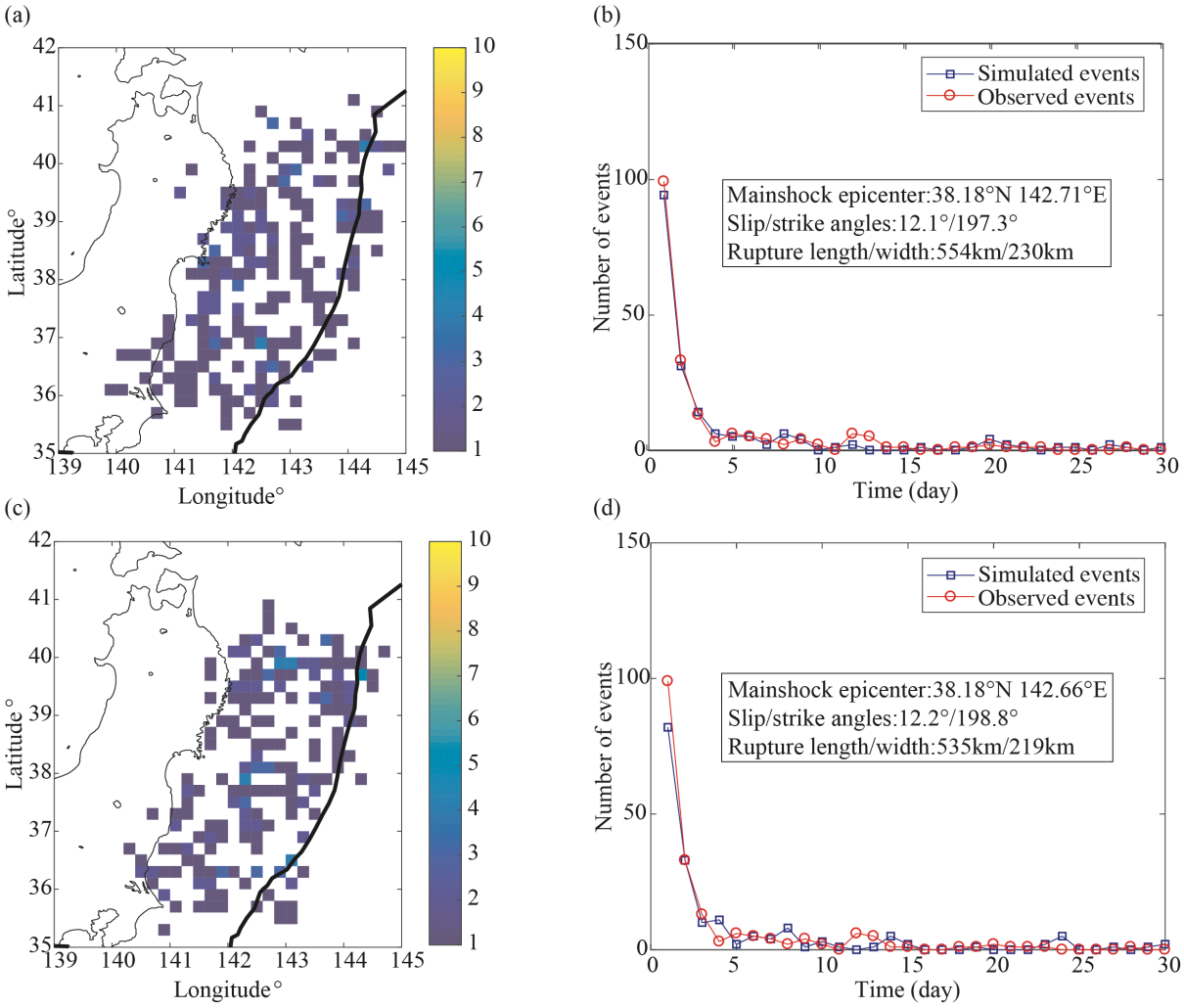

Figure 5. Two ETAS simulations in comparison with the 2011 Tohoku events with **M**≥5.5. (a, c) Simulated 2D aftershock histograms during the first 100 days. (b, d) Comparison of daily numbers of observed and simulated aftershocks. The mainshock source parameters (epicenter, slip angle, strike angle, rupture length, and rupture width) are randomly generated from the empirical distributions.

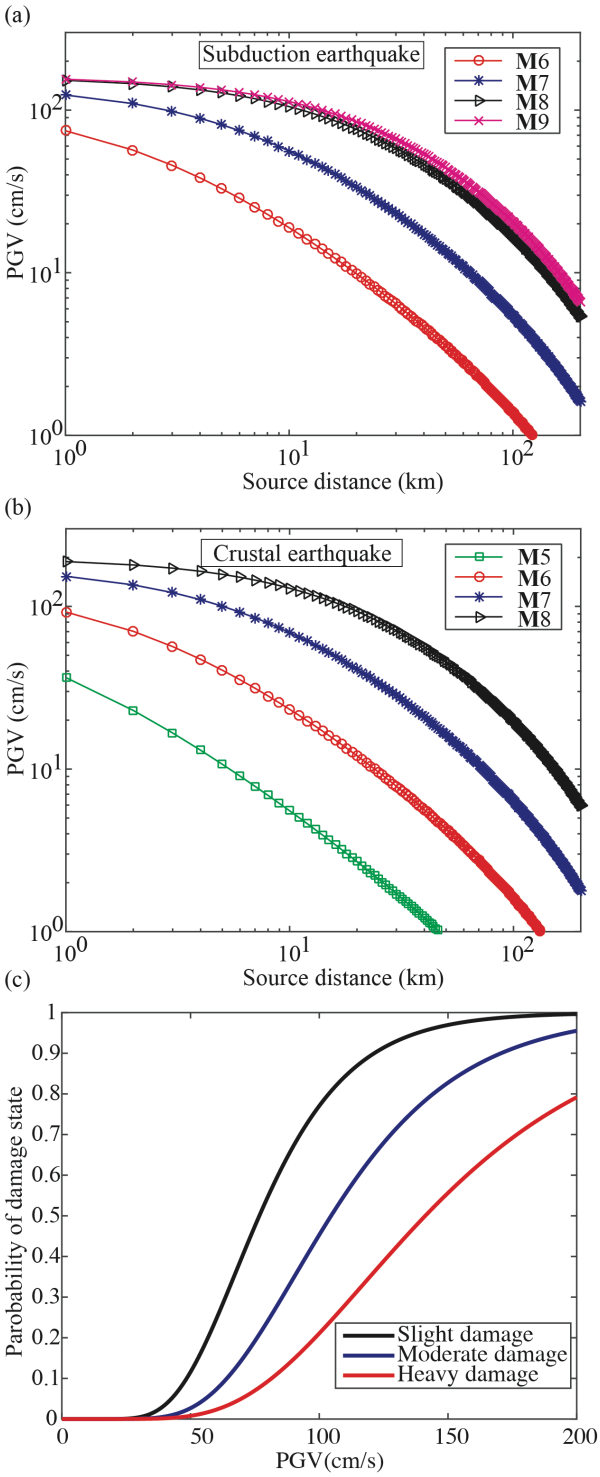

Figure 6. (a) Median values of PGV with V_{s30} = 300 m/s for subduction earthquakes from **M**6-**M**9 using the GMPE by Morikawa and Fujiwara (2013). (b) Median values of PGV with V_{s30} = 300 m/s for crustal earthquakes from **M**5-**M**8 using the GMPE by Morikawa and Fujiwara (2013). (c) Fragility curves (the probability of damage states against PGV) of wood-frame houses for Japan with slight damage, moderate damage, and heavy damage.

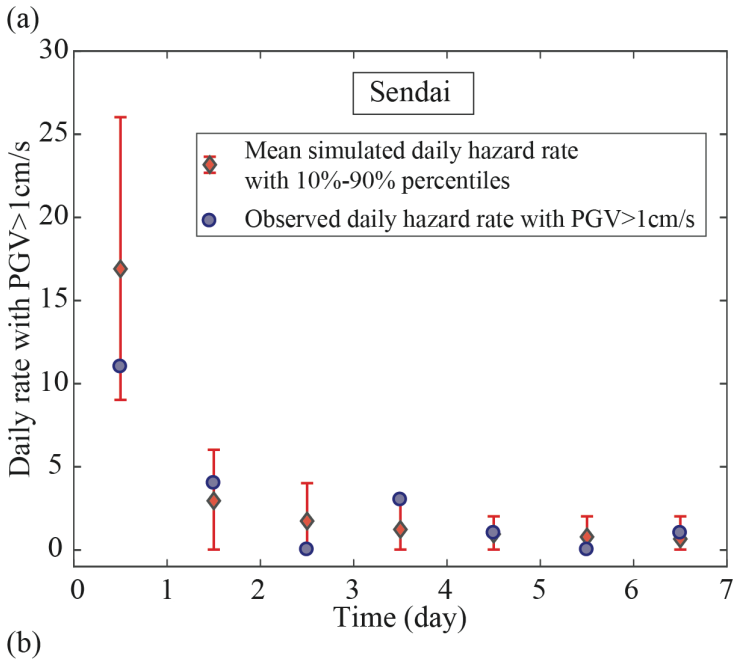
(a)
Sendai
Mean simulated daily hazard rate
with 10%-90% percentiles
Observed daily hazard rate with PGV>1cm/s
Daily rate with PGV>1cm/s
Time (day)

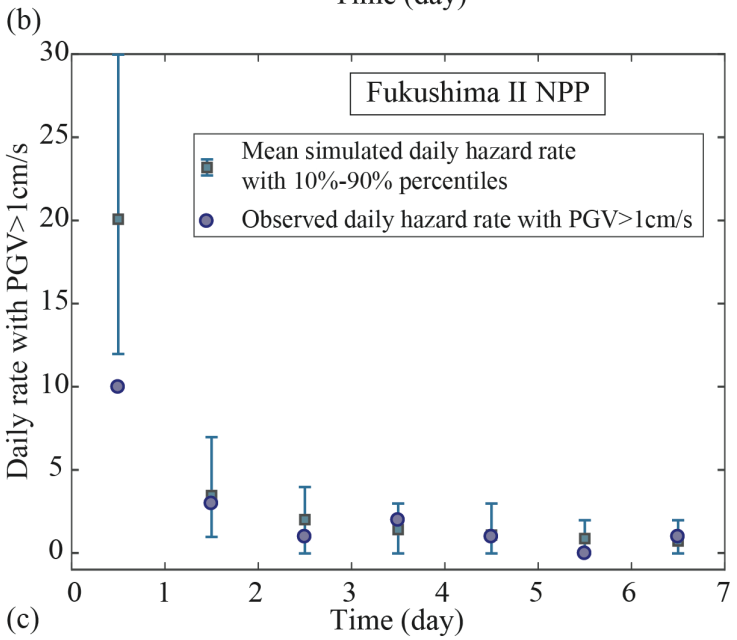
(b)
Fukushima II NPP
Mean simulated daily hazard rate
with 10%-90% percentiles
Observed daily hazard rate with PGV>1cm/s
Daily rate with PGV>1cm/s
Time (day)

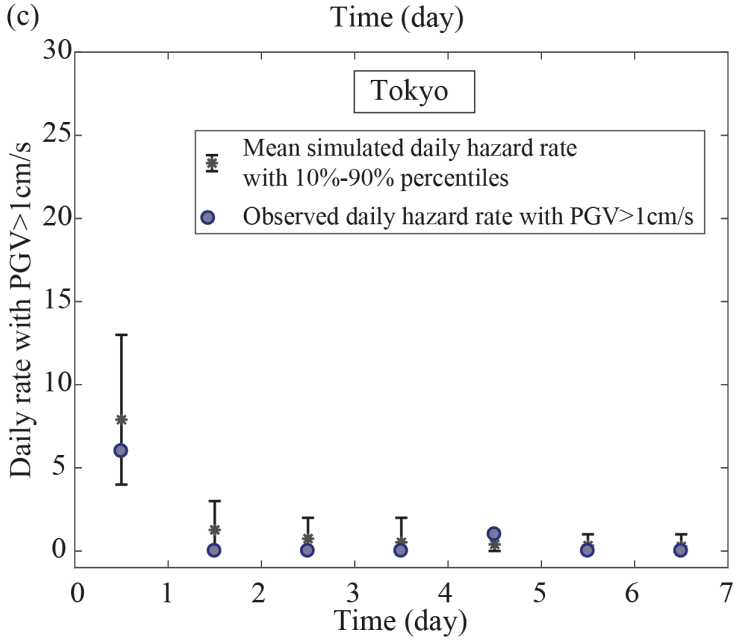
(c)
Tokyo
Mean simulated daily hazard rate
with 10%-90% percentiles
Observed daily hazard rate with PGV>1cm/s
Daily rate with PGV>1cm/s
Time (day)

1090

1091 **Figure 7.** Comparison of mean simulated and observed rate of PGV > 1 cm/s per day during
1092 the first 7 days after the 2011 Tohoku mainshock in (a) Sendai, (b) Fukushima II NPP and (c)
1093 Tokyo. Vertical bars denote 10th to 90th percentile range of simulated ground motions.
1094

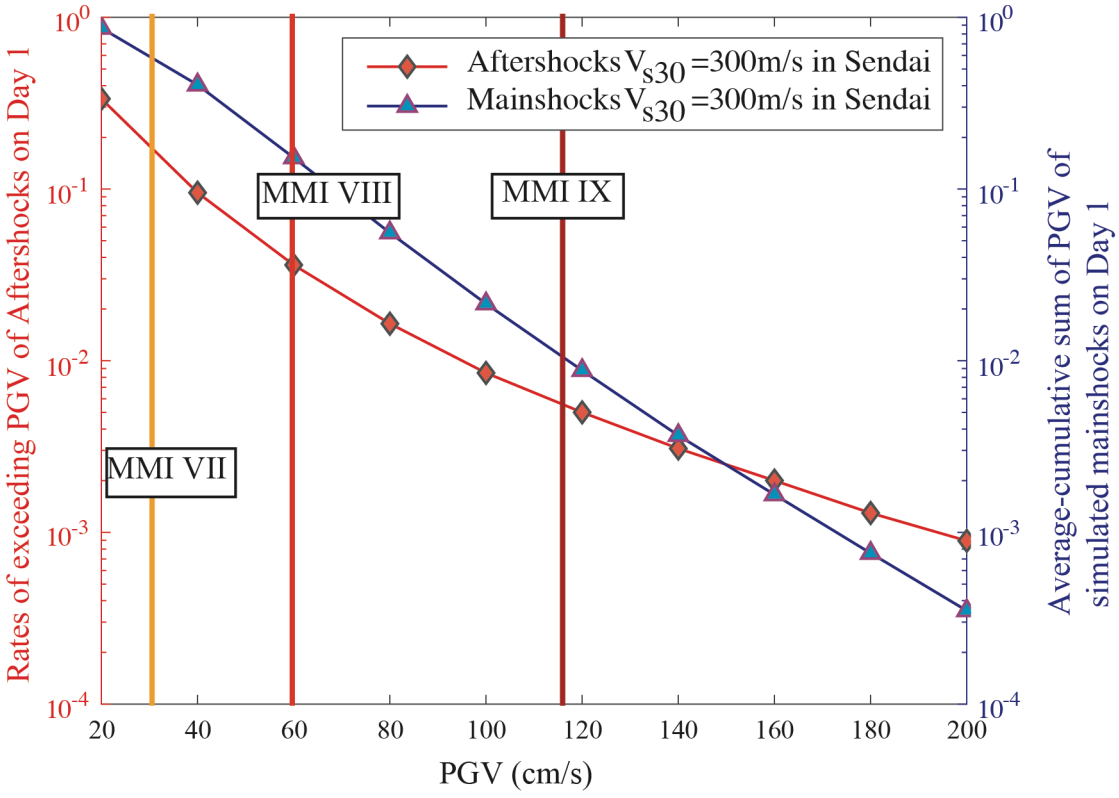

1095

1096 **Figure 8.** Rates of exceeding aftershock PGVs on left y-axis (diamond) on Day 1 in Sendai
1097 in comparison with PGV rates of simulated mainshock on right y-axis (upward-pointing
1098 triangle).

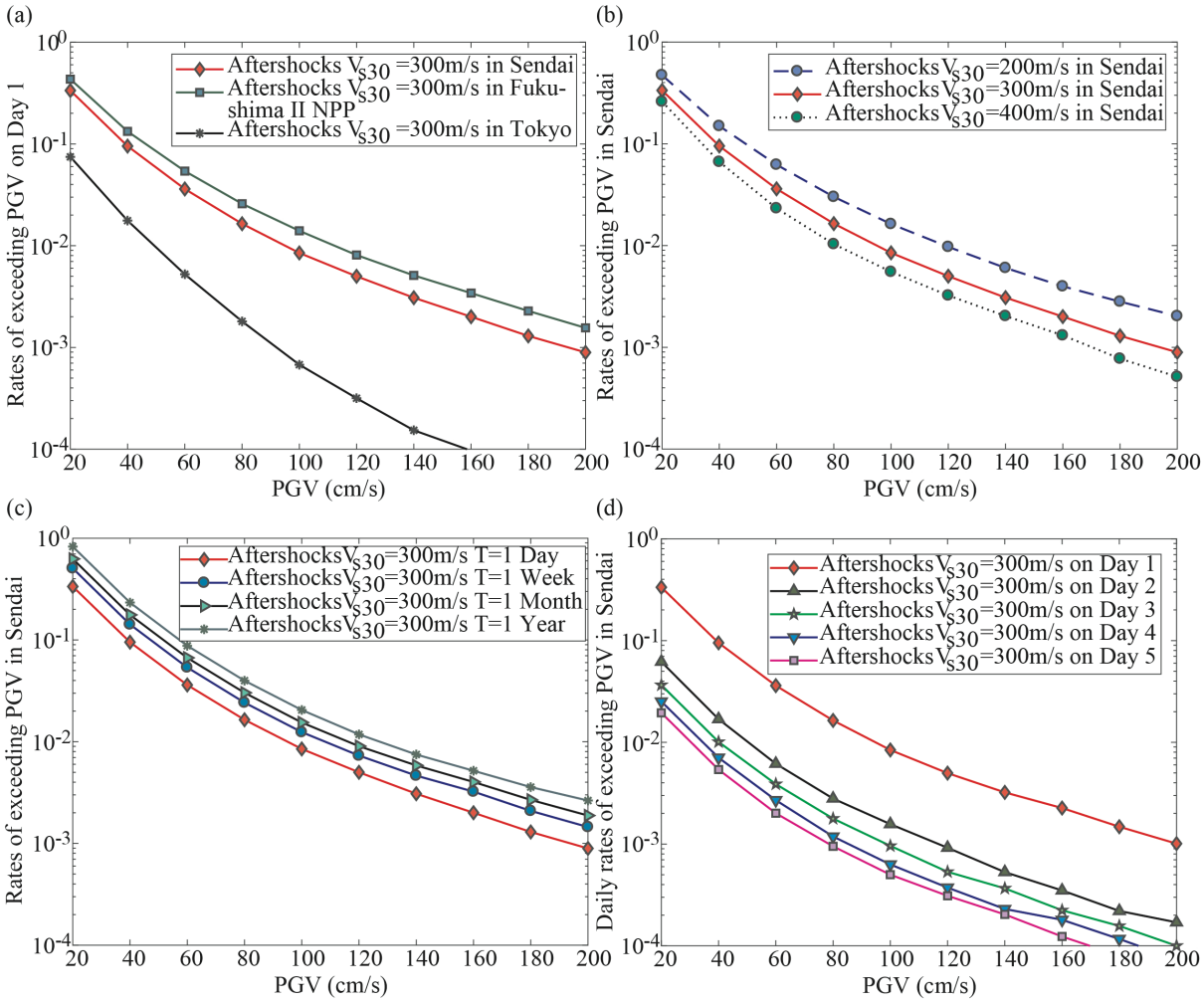

Figure 9. (a) Rates of exceeding aftershock PGVs (diamond) on Day 1 in Sendai in comparison with Fukushima II NPP (square), and Tokyo (star). (b) Three soil conditions with V_{s30} = 200 m/s (circle with dashed line), 300 m/s (diamond), and 400 m/s (circle with dotted line). (c) time periods with T = 1 day (diamond), 1week (circle), 1 month (right-pointing triangle), and 1 year (star). (d) Day 1 (diamond), Day 2 (upward-pointing triangle), Day 3 (pentagram), Day 4 (downward-pointing triangle), and Day 5(square).

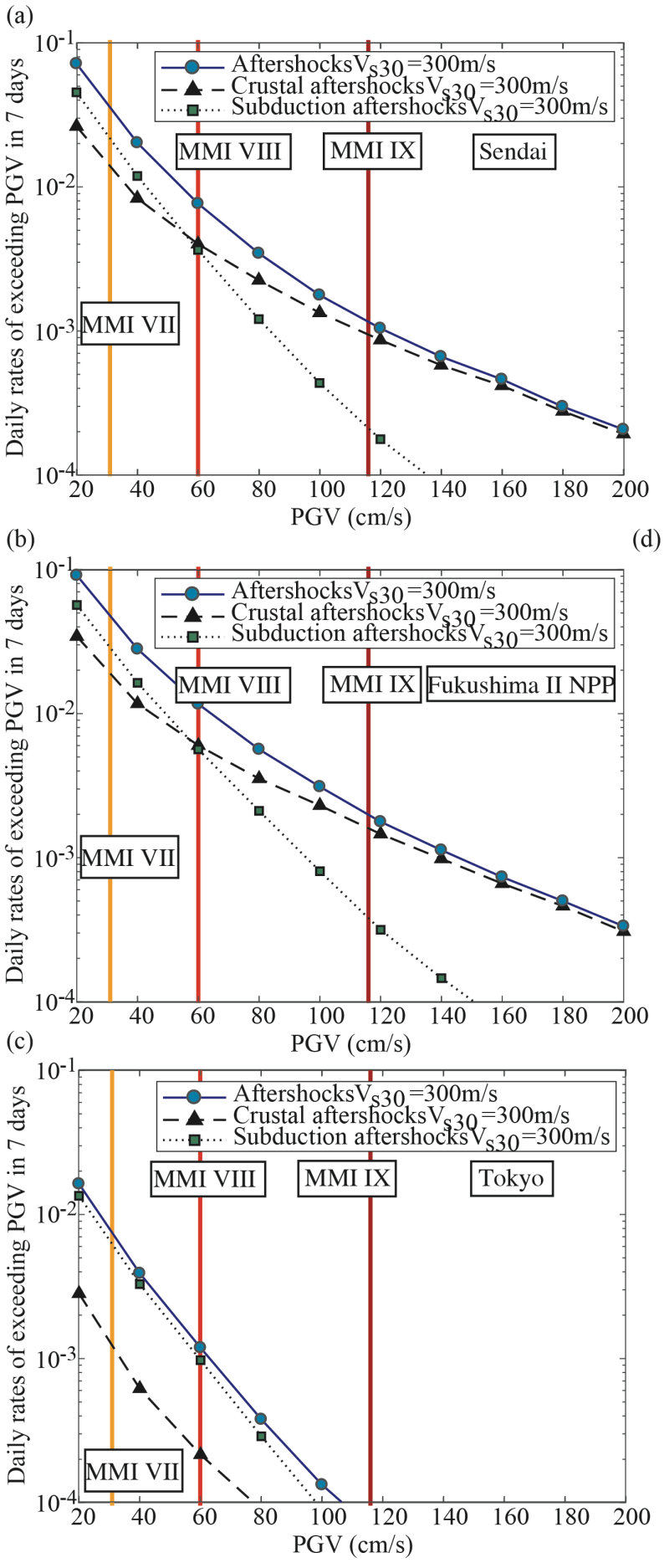
(a)
Aftershocks V_{S30}=300m/s
Crustal aftershocks V_{S30}=300m/s
Subduction aftershocks V_{S30}=300m/s
MMI VIII
MMI IX
Sendai
MMI VII
Daily rates of exceeding PGV in 7 days
PGV (cm/s)
(b)
(d)
Fukushima II NPP
(c)
Tokyo

Figure 10. Daily rates of exceeding PGV for crustal and subduction aftershocks (circles with solid line), crustal (upward-pointing triangles with dashed line) and subduction (squares with dotted line) aftershocks in the first 7 days in (a) Sendai, (b) Fukushima II NPP, and (c) Tokyo.

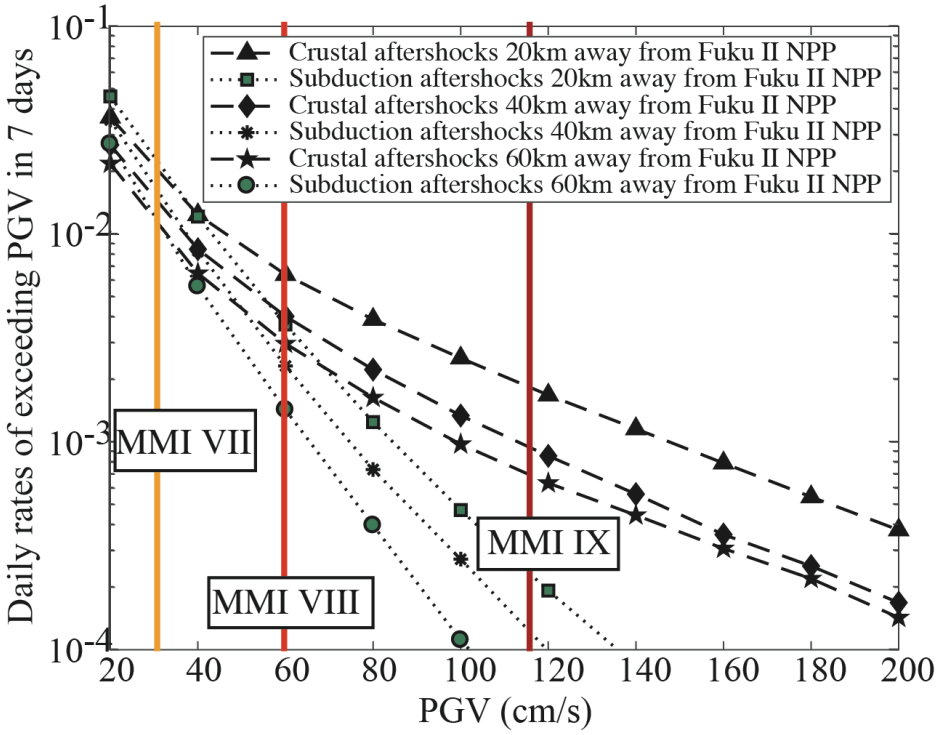

Figure 11. Daily rates of exceeding PGV for crustal and subduction aftershocks in the first 7 days 20km, 40km, and 60km away from Fukushima II NPP.

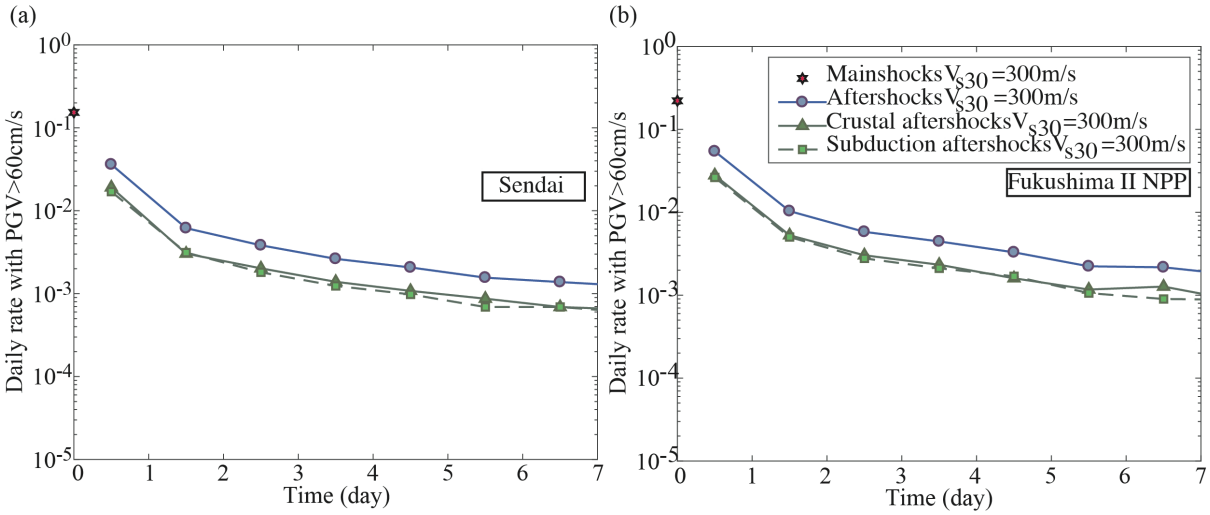

1115

1116 **Figure 12**. Daily hazard rates of PGV > 60 cm/s due to crustal and subduction aftershocks in

1117 comparison with simulated mainshock (stars) in (a) Sendai and (b) Fukushima II NPP.

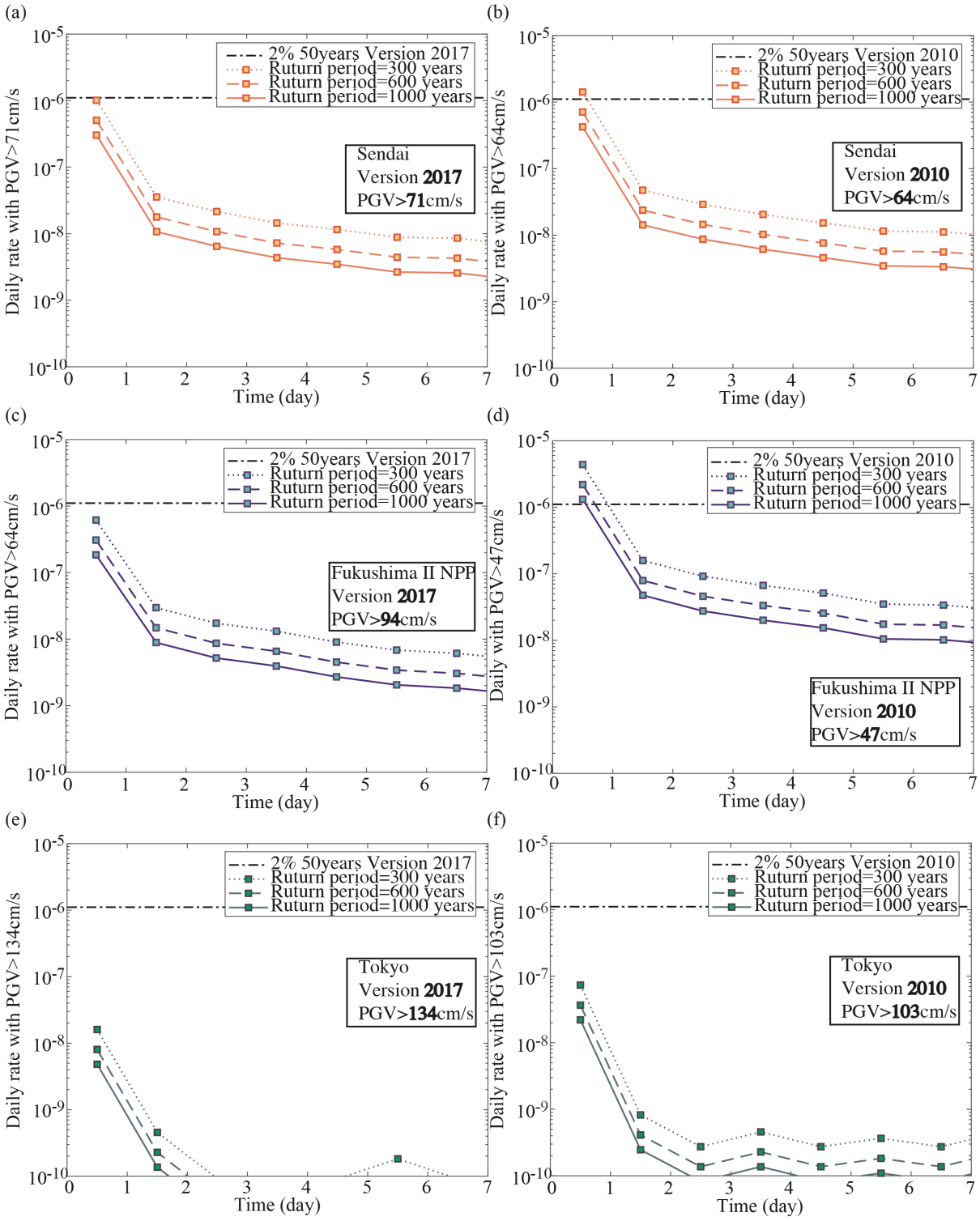

Figure 13. Left panels: comparison between daily time-dependent hazard rate (squares) and the 2017 JSHIS long-term hazard rate corresponding to 2% in 50 years (dash-dotted line) in (a) Sendai, (c) Fukushima II NPP, and (e) Tokyo. Panels in right column: corresponding comparisons with the 2010 JSHIS rate.

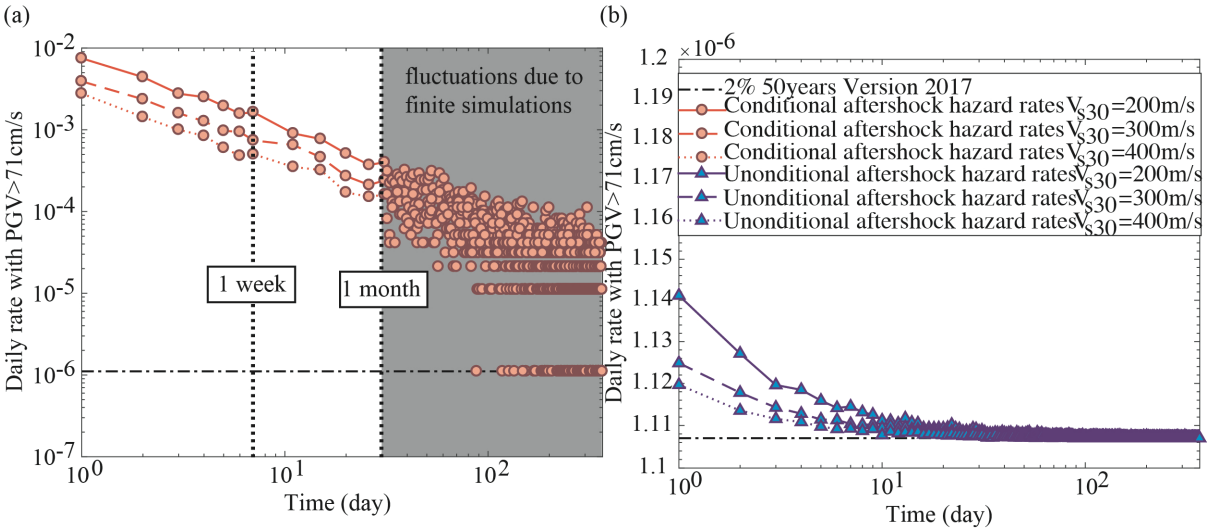

1123

1124 **Figure 14**. (a) Decay of conditional aftershock hazard rates in Sendai immediately after the

1125 Tohoku-like mainshock in one year. (b) Decay of unconditional aftershock hazard rates

1126 considering a 600-years return period of the Tohoku-like mainshock.

1127

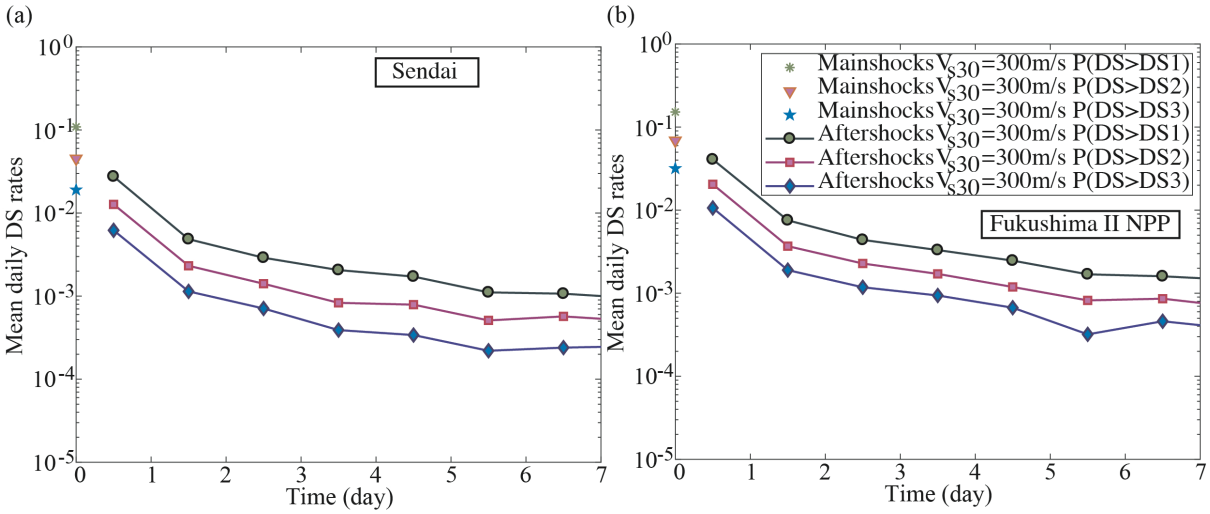

1128

1129 **Figure 15**. Comparison of mean daily DS rates of simulated mainshock and aftershocks in (a)

1130 Sendai and (b) Fukushima II NPP.

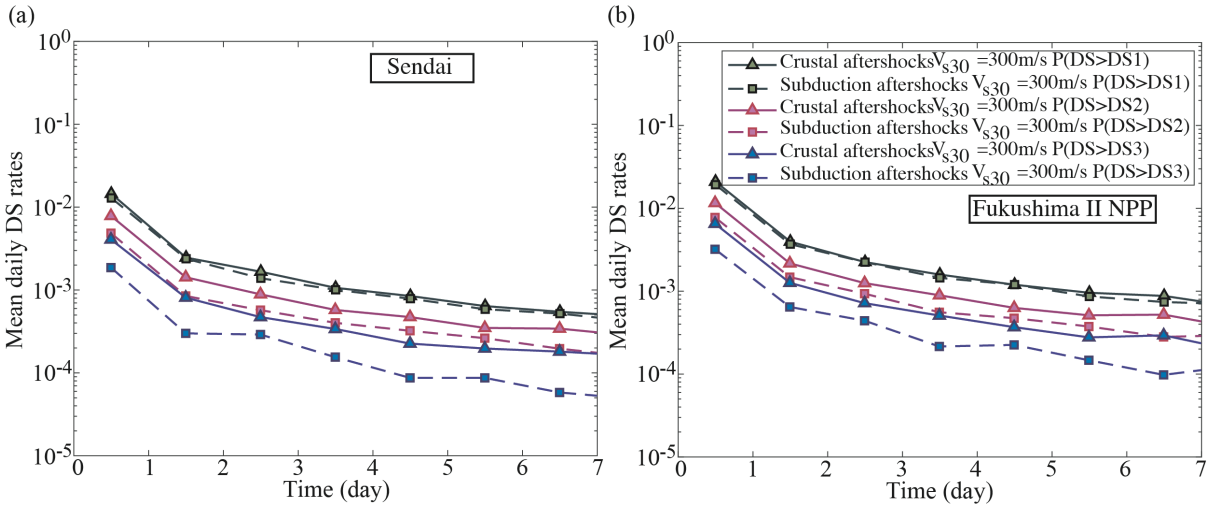

Figure 16. Mean daily damage state rates of crustal and subduction aftershocks for DS1, DS 2 and DS3 in (a) Sendai and (b) Fukushima II NPP.

Appendix 1

2D Gaussian distribution

Following Ogata (1998) and Ogata and Zhuang (2006), we assess the fit of a 2D Gaussian distribution to the spatial distribution of aftershocks. The anisotropic Gaussian distribution is defined by:

$$f_{A1}(x,y) = A\exp\left(-\left(\frac{(x-x_0)^2}{2\sigma_x^2}\right) + \left(\frac{(y-y_0)^2}{2\sigma_y^2}\right)\right) \quad \text{(A1)}$$

where A is a constant, x and y are the locations of earthquakes, σ_x and σ_y are the standard deviations, and x_0 and y_0 are the averaged locations of the aftershocks. In the simulation framework, x_0 and y_0 are assumed to equal the mainshock epicenter of a bilateral rupture area. The sampled rupture length and width from the empirical scaling law (Thingbaijam *et al.*, 2017) can be applied to the 2D Gaussian distribution by scaling the standard deviations. An example of the probability density function (PDF) with rupture length and width (500km×300km) is shown in **Figure A1**. While the anisotropic 2D Gaussian aftershock distribution offers several advantages, we do not employ it here. First, the 2D Gaussian distribution decays faster than the power law near and beyond the boundaries of the rupture area, which does not represent the spatial aftershock distribution well (Felzer and Brodsky, 2006). Second, in comparison with the observed 2D aftershock histogram of the 2011 Tohoku sequence in **Figure 3**(d), the 2D gaussian distribution with a high rate in the center point does not have a good with the observed catalog.

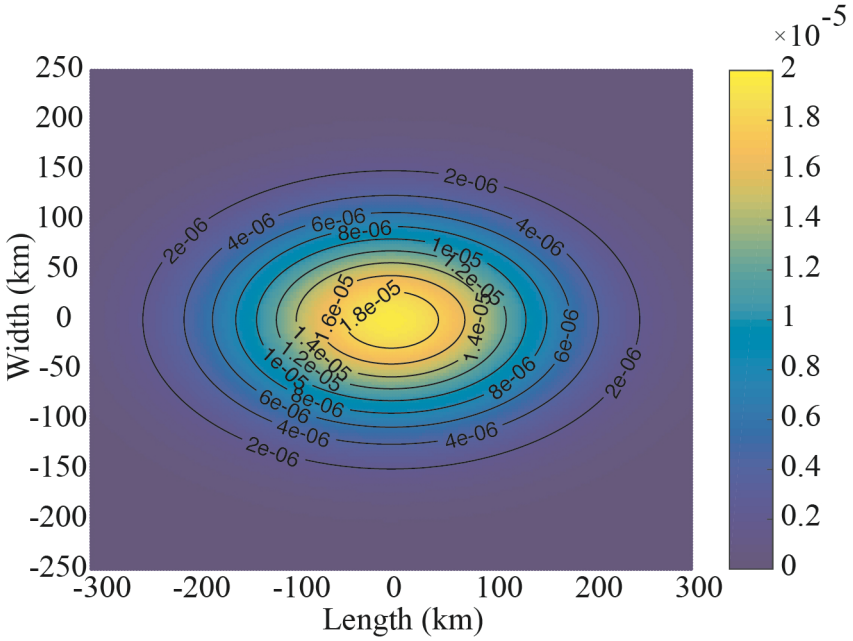

1155

1156 **Figure A1.** An example of the spatial PDF of the first generation of aftershocks with a

1157 simulated rupture area (500 km×300 km).

1158

1159 *Anisotropic power law distribution*

1160 We also considered an anisotropic power law kernel to simulate the spatial distribution of

1161 aftershocks (Kagan and Jackson, 1994; Wang *et al.*, 2011; Ramanna and Dodagoudar, 2012).

1162 $$f_{A2}(x,y) = \frac{1}{\pi h^2}\frac{1+\delta cos^2\phi}{1+\delta/2}\left(1+\frac{x^2+y^2}{h^2}\right)^{-2} \quad \text{(A2)}$$

1163 where h is the kernel bandwidth which is identical to the bandwidth from Equations (6) and

1164 (7), ϕ is related to the strike angle of the fault plane and δ determines the length-width ratio of

1165 the mainshock rupture area. An example of the plot of PDF with rupture length and width

1166 (500km×300km) is shown in **Figure A2**. However, because of the irregular shape in **Figure**

1167 **A2**, the spatial aftershock rates along the mainshock rupture length could be underestimated.

1168 Therefore, anisotropic Kernel power law is not appropriate for spatial aftershock

1169 distributions.

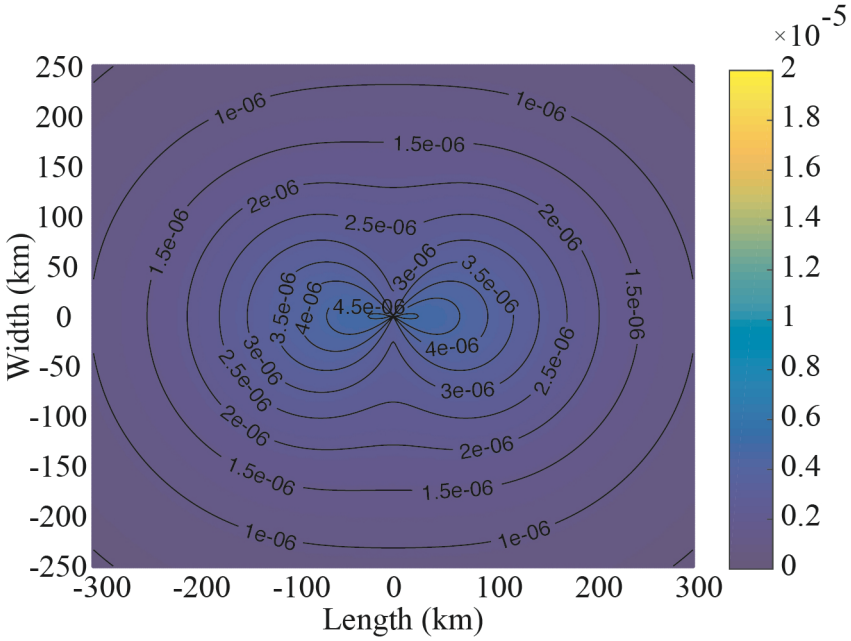

1170

1171 **Figure A2.** An example of the spatial probability density function of the first generation of

1172 aftershocks with a simulated rupture area (500 km×300 km).

1173

1174

Appendix 2

Daily hazard rate from JSHIS

The 2% long-term hazard map in 50 years from JSHIS is estimated by a Poisson distribution:

$$P_A = 1 - e^{-\lambda_A t_A} \quad \text{(A3)}$$

where P_A is the probability that a given intensity measure could be exceeded in t_A years with an annual occurrence rate of λ_A. In **Figure 13** and **Figure 14**, the daily hazard rate (λ_{JSHIS}) based on the long-term hazard map from JSHIS is calculated by:

$$\lambda_{JSHIS} = \ln\left(\frac{1}{1-P_A}\right) \times \frac{1}{t_A} \times \frac{1}{N_{days}} \quad \text{(A4)}$$

where N_{days} is the number of days in one year. λ_{JSHIS} is shown in **Figure 13** and **Figure 14** with dash-dotted lines.

Daily mainshock-aftershock hazard rate from the ETAS model

The daily mainshock-aftershock hazard rate $\lambda_{MsAs}(t)$ on day t in **Figure 13** (both 2010 and 2017 versions) is estimated from the aftershock hazard rate given the mainshock occurs from the ETAS model multiplying by the daily rate of the mainshock, and is calculated by:

$$\lambda_{MsAs}(\mathrm{t}) = \lambda_{Ms} \times \lambda_1(PGV_{MsAs}(\mathrm{t}) \geq PGV_{JSHIS}|\mathrm{Ms}) \times \frac{1}{N_{days}} \quad \text{(A5)}$$

where λ_{Ms} is the annual rate of the Tohoku-like mainshock considering different return periods; λ_1 is the conditional daily exceedance hazard rate of mainshock-aftershock sequences given that the mainshock occurs; $PGV_{MsAs}(t)$ is the rate that the simulated PGVs $\geq PGV_{JSHIS}$ on day t from the hazard analysis. PGV_{JSHIS} shows that the probability the PGVs in 50 years is exceed PGV_{JSHIS} is 2%. For example, PGV_{JSHIS} from the 2017 JSHIS hazard map in Sendai is 71 cm/s.

Daily conditional and unconditional aftershock hazard rates

In **Figure 14** daily conditional ($\lambda_{con}(t)$) aftershock hazard rates is the daily aftershock rate right after the mainshock occurs, and daily unconditional ($\lambda_{uncon}(t)$) aftershock hazard rates is the daily aftershock rate given the mainshock occurs multiplying by the daily rate of the mainshock. Daily conditional ($\lambda_{con}(t)$) and unconditional ($\lambda_{uncon}(t)$) aftershock hazard rates in are calculated by:

$$\lambda_{con}(\mathrm{t}) = \lambda_{JSHIS} + \lambda_2\left(PGV_{As}(\mathrm{t}) \geq PGV_{JSHIS} \middle| \mathrm{Ms}\right) \quad \text{(A6)}$$

$$\lambda_{uncon}(\mathrm{t}) = \lambda_{JSHIS} + \lambda_{Ms} \times \lambda_2\left(PGV_{As}(\mathrm{t}) \geq PGV_{JSHIS} \middle| \mathrm{Ms}\right) \times \frac{1}{N_{days}} \quad \text{(A7)}$$

where λ_{JSHIS} is considered as the background rate from Equation (A4). λ_{Ms} is the annual rate of the Tohoku-like mainshock considering different return periods. λ_2 is the conditional daily exceeding hazard rate of aftershocks given the mainshock occurs. $PGV_{As}(t)$ is the rate that the simulated PGVs of aftershocks $\geq PGV_{JSHIS}$ on day t from the hazard analysis. $\lambda_{con}(t)$ and $\lambda_{uncon}(t)$ are shown as upward-pointing triangle and circle, respectively, in **Figure 14**.